CHALMERS
UNIVERSITY OF TECHNOLOGY

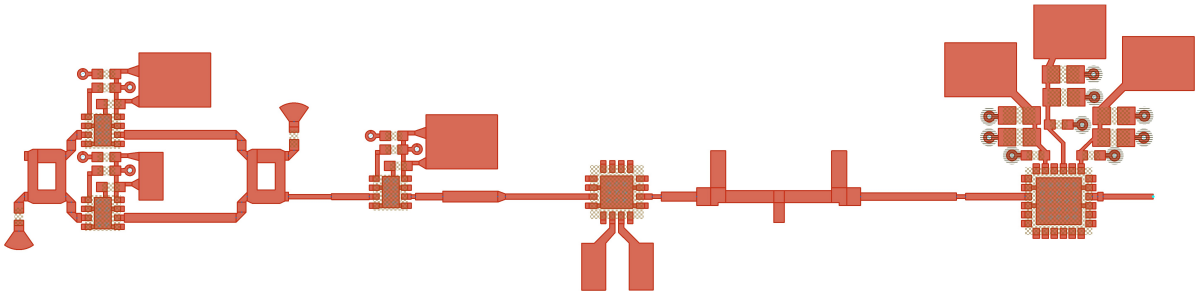

An Exploration of Low-Cost LNA Systems Intended for LEO Satellites

Master's thesis in Embedded Electronic System Design

FELIX BRATT & JAKOB HENNINGSSON

Department of Microtechnology and Nanoscience
CHALMERS UNIVERSITY OF TECHNOLOGY
Gothenburg, Sweden 2025

Master's thesis 2025

An Exploration of Low-Cost LNA Systems intended for LEO Satellites

FELIX BRATT
JAKOB HENNINGSSON

Department of Microtechnology and Nanoscience
Chalmers University of Technology
Gothenburg, Sweden 2025

An Exploration of Low-Cost LNA Systems intended for LEO Satellites
FELIX BRATT
JAKOB HENNINGSSON

Supervisor: Per Larsson-Edefors, Department of Microtechnology and Nanoscience
Company advisor: Dennis Kleen and Peter Alsholm, Beyond Gravity - Electronic Solutions
Examiner: Lena Peterson, Department of Microtechnology and Nanoscience

Master's Thesis 2025
Department of Microtechnology and Nanoscience
Chalmers University of Technology
SE-412 96 Gothenburg
Telephone +46 31 772 1000

Cover: The final layout for one of the explored low-cost LNA systems.

Typeset in LaTeX
Gothenburg, Sweden 2025

An Exploration of Low-Cost LNA Systems intended for LEO Satellites
FELIX BRATT & JAKOB HENNINGSSON
Department of Microtechnology and Nanoscience
Chalmers University of Technology

Abstract

The increasing demand for low-latency, on-demand services has warranted the transformative shift from satellites placed in geostationary orbit (GEO) to low Earth orbit (LEO). To achieve coverage comparable to that of GEO satellites, LEO satellite constellations such as Starlink require thousands of satellites, potentially leading to substantial costs if using traditional space-qualified electronics. However, compared to those in GEO, the less stringent reliability requirements for satellites in LEO have sparked interest in identifying low-cost solutions for various system modules, including low-noise amplifier (LNA) systems.

This project seeks to explore low-cost alternatives to the K_a-band LNA hybrid developed at Beyond Gravity in Gothenburg. These alternatives were to be based on commercial off-the-shelf (COTS) components, commercial printed circuit board (PCB) materials, and various design strategies aimed at reducing the overall system cost. The project aimed to compare these cost-effective alternatives with a current high-reliability implementation, to assess the design trade-offs between cost and performance. Also, the project aimed to establish what criteria a design option must fulfil to be deemed suitable for use in LNA systems intended for LEO satellites, as well as highlight the industry-related challenges that hinder the full adoption of the New Space paradigm.

The design process consisted of distinct phases, ranging from an initial screening of possible component configurations to the design and optimisation of the final system implementations. The project resulted in two system alternatives: one that incorporates the existing WR28 isolator and has the potential to reduce costs to approximately one-fourth of the original design, and another that explores a system using a quadrature hybrid coupler (QHC) configuration, which offers a tenfold reduction in cost. We believe that the greatest potential to reduce cost lies in replacing the expensive isolators. However, the primary challenge is to maintain sufficient return loss without compromising the system's noise figure.

Keywords: LNA systems, LEO satellites, New Space, COTS components, Commercial PCB materials, K_a-band, WR28 isolators, Noise figure, Return loss, OIP3, Quadrature hybrid couplers

Acknowledgements

We want to start by first thanking everyone at Beyond Gravity, whom we have been fortunate to work with and for the amazing opportunity to conduct our thesis in collaboration with you. Thank you, Dennis and Peter, for supervising us and for your continuous support throughout this semester. Also, many thanks to Richard, Marita, Jan, Herman, Andreas, Jonas and Michael for all of your individual contributions, we appreciate it a lot!

We also want to give huge thanks to Per and Lena, our supervisor and examiner at Chalmers. Thank you for your insights, feedback on our work and for always being available to assist us!

Felix - I want to give personal thanks to my wonderful fiance Alva, my friends and family, whose support and encouragement have always motivated me to push myself further. I also want to thank all the energy drinks and cups of coffee which has sustained me with the energy needed to carry we throughout these five years (+a gap year)!

Jakob - I want to give special thanks to Alice, my friends and my family, who have been willing to listen to me while I complain about deadlines and early mornings, as well as the continuous support and motivation to do my absolute best.

Felix Bratt & Jakob Henningsson, Gothenburg, June 2025

Acronyms

BP	BandPass
BS	BandStop
BW	BandWidth
COTS	Commercial Off The Shelf
EM	ElectroMagnetic
FR4	Flame Retardant 4
GEO	Geostationary Orbit
HEMT	High Electron Mobility Transistor
Hi-Rel	High-Reliability
HMC	HMC519LC4
IP3	Third-Order Intercept Point
LEO	Low-Earth Orbit
LNA	Low Noise Amplifier
LP	Low-Pass
MAAL	MAAL-011238
MAAV	MAAV-011013
MMIC	Monolithic Microwave Integrated Circuits
MOSFET	Metal Oxide Silicon Field-Effect Transistor
OIP3	Output Third-Order Intercept Point
PCB	Printed Circuit Board
PCL	Parallel-Coupled Line
QHC	Quadrature Hybrid Coupler
RF	Radio Frequency
RL	Return Loss
S	Scattering
SEL	Single Event Latch-up
SEU	Single Event Upsets
TEM	Transverse ElectroMagnetic
TID	Total Ionising Dose

Contents

1

Introduction

Millions of people today rely on on-demand services for entertainment, news, information, and convenience in their daily lives. One category that has seen a rapid surge in its user base is video streaming platforms [1]. These platforms reached new heights during the COVID-19 pandemic, when they served as the primary source of entertainment for many people who had to or chose to isolate themselves in their homes [2]. This has all accumulated into millions of video streaming users across the world. In their financial report of the final quarter in 2024, Netflix alone reports that over 300 million people are signed up for their services, which marked a 15% increase from the year before [3].

As on-demand broadcasting continues to grow and platform owners seek to support more users, there is an increasing demand for lower-latency wireless communication [4]. This demand is especially important as many of the mentioned platforms have started to incorporate live broadcasting, such as sports events, into their services [5]. Much of the telecommunication that broadcasting services rely on today utilises large satellites placed in geostationary orbit (GEO) which has an altitude of about 36 000 km above the Earth [6]. Due to their high altitude, it is possible to achieve coverage of most of the world with just three satellites. While their distance provides extensive global coverage, the latency caused by the long transmission distance necessitates the shift toward faster interconnections and lower latencies.

In 2019, Starlink made a significant leap in satellite technology when they launched and established their large-scale constellation of low Earth orbit (LEO) satellites [7], propelling the world into the *New Space* era. This orbit's altitude is about 550 km above the Earth, which allows for more than 20 times lower latency than that of the satellites placed in GEO [8]. The main issue, however, with constellations such as Starlink is that they require thousands of satellites to obtain coverage on par with a GEO satellite. Because satellites must withstand the harsh environment of space and cannot be repaired in case of malfunction, they must be highly durable and well-designed to ensure an acceptable lifespan. This desired robustness for thousands of satellites comes at a high manufacturing cost, prompting researchers and manufacturers to explore new approaches for developing low-cost satellite designs for use in LEO.

1.1 Background

In the New space era, which promotes commercialism, collaboration and innovation within the space industry, commercial-off-the-shelf (COTS) components have recently become a central subject in research discussions as replacements for the traditional space-qualified components [9]. Their appeal lies not only in their affordability but also in their capacity to enable faster development cycles, as they are readily available from vendors and have been thoroughly tested by their manufacturers. This appeal has quickly prompted researchers to investigate their validity in space applications. While some argue that their use is almost mandatory [10], many researchers are concerned about their reliability, specifically their ability to withstand radiation [11], [12]. Space is a hostile environment and, currently, there exists no straightforward procedure to service a commercial satellite once it has been deployed.

However, the level of acceptable system reliability differs between satellites placed in LEO versus GEO. A satellite in GEO has a required lifespan of about 15-18 years, whereas satellites in LEO cannot live longer than approximately seven years, as a result of orbital degradation [13]. In other words, LEO offers the potential of using components with a shorter lifespan than what would be required for satellites in GEO. Another consideration is that the majority of Earth's coverage with a satellite constellation in LEO can remain intact, even if a large fraction of the satellites were to malfunction. In contrast, if only one GEO satellite were to malfunction, a third of the total coverage would be lost. Thus, due to the less stringent reliability requirements for LEO satellites compared to those in GEO, many researchers and industry professionals see significant potential in COTS components as a means to reduce manufacturing costs.

One company that has taken a special interest in the potential of COTS components for space applications is Beyond Gravity. They are a major supplier of both satellite solutions and launch vehicle structures, with its main headquarters located in Zürich, Switzerland [14]. In Gothenburg, the company operates a large facility where they research and develop high-reliability electronic products, such as digital electronics, microwave electronics, and antennas [15]. One particular product developed in their Gothenburg office is the *K_a-band low-noise amplifier (LNA) Hybrid*, an LNA system designed for frequencies within 27–31 GHz [16]. LNAs are essential components in wireless systems such as satellites. They are often used in receivers to amplify weak received signals while keeping inserted noise at a minimum [17].

Traditionally, these systems are designed at Beyond Gravity using *multi-chip module* (MCM) technology, also known as *hybrids*, with bare *monolithic microwave integrated circuits* (MMICs) manually mounted onto the substrate [16]. This allows for LNA systems with high performance, bandwidth and reliability. However, their high material costs and extensive screening procedures necessitate a more cost-effective design better suited for LEO satellites. Of particular interest is the potential of basing the design on encapsulated COTS components and commercial printed circuit board (PCB) materials, while also evaluating the trade-offs in performance and cost. This would also allow the system to be better suited for automated manufac-

turing. Currently, assembling one system by hand takes approximately one week, but if switched to automated manufacturing it is estimated that productivity would increase by a factor of ten. This presents an opportunity to explore new design approaches and methodologies for electronics in the New Space era.

1.2 Related Work

This section reviews related works discussing the use of COTS components in space applications. First, we examine researchers' investigations into the validity of these components for space use, as introduced in Section 1.1. Specifically, we highlight the components' susceptibility to radiation-induced faults and potential consequences for the system as a whole. The second part outlines Pignol et al. proposed procedure of how researchers and developers can evaluate a COTS component [18]. This subsection also brings up the discussion of thorough testing procedures and at what level they can be simplified to bring down the cost.

1.2.1 Radiation Resilience of COTS Components

One of the most frequently brought up issues with COTS components is that they are much more susceptible to radiation, which in turn makes the overall system more vulnerable to radiation-induced faults [11]. *Single event effects*, for example, is a category of radiation-induced faults that are a result of high-energy particles colliding with electronic components [12]. These events may cause issues that range from temporary system resets and incorrect data (*single event upsets* (SEU)) to permanent damages to the component (*single event latch-up* (SEL)). Another category is *total ionising dose* (TID), which is an accumulation of ionising radiation that damages the components over time. This accumulation may severely degrade the components' performance or cause them to malfunction. It is therefore important to select the COTS components with care, otherwise, as [11] comments, the security and integrity of the entire system may be compromised.

1.2.2 Selection Procedure of COTS Components

While most publications highlight the risks associated with the reliability of using COTS components [11], [12], few offer a structured approach for assessing their appropriateness. An exception can be found in one of the discussion chapters written by Pignol et al. in [18], where a three-step procedure is proposed.

The first step, referred to as the *selection step*, starts by surveying the market for available components that meet the targeted system specifications, such as quality, performance and cost. Components that show promise should then be reviewed in consultation with experts in different fields, as well as representatives from both the design and product assurance teams, to ensure that all necessary requirements are fulfilled. Following this, the *procurement step* can be carried out where samples of the promising components are obtained, along with traceability documentation from the manufacturer. The authors emphasise that this step is crucial to ensure traceability of the entire system and to prevent the use of any counterfeit components.

The final step is called the *lot acceptance test step* and involves a series of different performance and quality tests of the components. The testing procedures to be carried out should include the following:

- electrical characterisation at three temperatures,
- construction analysis to confirm the manufacturing quality,
- life-cycle test on the components' long-term reliability,
- thermal cycling test related to the system profile,
- screening test/burn-in to eliminate early failed components,
- electro-magnetic compatibility in conductive susceptibility,
- on/off power cycling test for missions where it is important to optimise power consumption,
- damp heat test,
- radiation test based on the radiation environment (TID, SEL and SEU).

In other words, a considerable number of steps must be performed before a COTS component can be considered suitable for space applications. On the other hand, Pignol et al. do encourage designers to tailor the testing procedure to the specific system requirements, and when appropriate, reduce them to strike a better balance between system quality and cost.

The discussion of how thorough testing procedures should be conducted is also brought up by Jaime Estela [19]. He provides a critical perspective of researchers and developers who has the tendency of reducing the number of tests as a means to bring down cost. One crucial aspect of COTS components, which he highlights, is that their datasheets rarely detail any information regarding the device's resilience to radiation. Additionally, while the maximum operating ratings are often specified within certain temperature ranges, there is often no data on how the component behaves beyond them. According to Estela, the issue is not whether a component can survive in space or not, but rather how long and at what limits it can continue to operate properly. Thus, in contrast to the other authors, he encourages researchers and developers to conduct many thorough, comprehensive tests to fully understand the true boundaries of the components. He remarks on the common notation made by many researchers that once a system is launched into space, repairing it is not an easy feat.

1.3 Research Gap

As highlighted in Section 1.2, there currently exists no universally accepted framework for the proper selection of COTS components intended for space applications. Much of the existing research focuses on the importance of component reliability and its resilience against radiation, as well as the extensive testing procedures that should be undertaken to ensure their appropriateness. There are also differing opinions on how rigorous the testing procedures need to be in order to assess a COTS component's suitability for an intended space application.

However, few studies address the design limitations that could prevent COTS components from delivering the required system performance. This is particularly true in the context of LNA systems operating within the K_a-band. Although a few studies, such as the article by Ali et al. [20], explore LNA systems built with COTS components, these are typically designed around the S-band (2–4 GHz). As we move up in frequency, we expect new challenges to arise, especially concerning the interconnections of the commercial components. Moreover, publications such as [20] only provide a high-level overview of the system and leave out valuable insights regarding the design process, including methods used, choices made and constraints faced. Additionally, most publications rarely offer any quantitive assessment of how cost may differ between LNA systems intended for LEO versus GEO satellite applications.

1.4 Overview of the Hi-Rel LNA-System

The high-reliability (Hi-Rel) K_a-Band LNA Hybrid by Beyond Gravity is designed for telecommunications payloads operating within 27 to 31 GHz [16]. While the design targets a 4 GHz passband, not all of the covered frequencies are intended for commercial systems, though the majority are. Its system chain, illustrated in Figure 1.1, consists of four MMIC LNAs, two commercial MMIC attenuators, and one parallel-coupled line (PCL) bandpass (BP) filter, attenuating frequencies above and below the specified band. The most important feature of the BP filter is attenuating the lower frequencies, 17 to 22 GHz, at which the signal should be attenuated by at least 50 dB. The system chain also includes two WR28 waveguides and two relatively expensive WR28 compatible isolators. WR28 is a waveguide dimension standard which corresponds to frequencies ranging from 26.5 to 40 GHz [21].

The two attenuators are regulated by an external gain control and temperature compensation system. Said system sets the specific total gain of the system, ranging from 40 to 55 dB. These attenuators are also used to ensure substantial *gain stability*, which is the system's robustness against temperature-induced fluctuations in gain. When the temperature drops in the system, the transistors in the LNAs operate faster, which increases their amplified gain. This increase in gain is cumulative across all the system components, which may add up to an excessive deviation from the target gain.

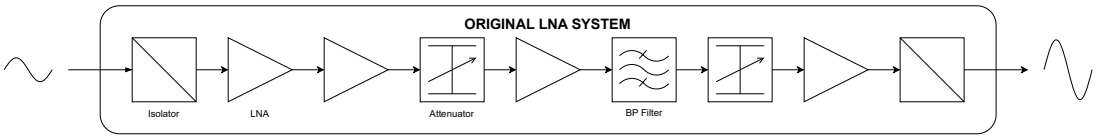

Figure 1.1: The original LNA RF chain designed for the K_a-band.

The system can also be designed as a low-gain version, presented in Figure 1.2, which removes the second amplifier and the first attenuator.

All MMICs are wire-bonded bare dies, and while we are not permitted to disclose the exact components or their specifications, Table 1.1 lists representative value ranges that the components fall within. Figure 1.3 showcases the physical layout of the

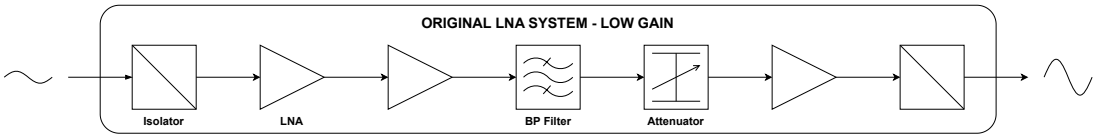

Figure 1.2: The original, low-gain LNA RF chain designed for the K_a-band.

high-gain Hi-Rel system which is slightly blurred to not expose the full details of its design.

Table 1.1: Representative value ranges for the bare die MMIC utilised in the K_a-Band LNA Hybrid.

Metric	**Value Range**
LNA components	
Noise figure (dB)	1 - 3.5
Gain (dB)	15 - 25
OIP3 (dBm)	15 - 30
Supply voltage (V)	3
Attenuators	
Insertion loss (dB)	2 - 4
Attenuation range (dB)	15 - 40
Supply voltage (V)	3

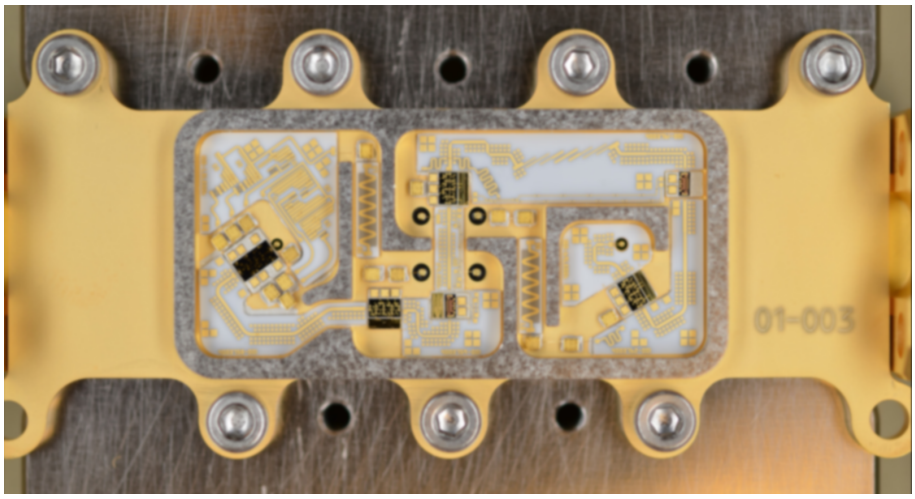

Figure 1.3: Physical layout of the Hi-Rel K_a-band LNA-System.

1.5 Purpose and Goal

The purpose of this thesis is to explore how to design a low-cost LNA system for high-volume satellite constellations deployed in LEO, and to assess the trade-offs between cost and performance. This thesis also seeks out to identify and discuss the potential constraints that may hinder the industry's full embrace of the trends shaping the New Space era. This was carried out with the goal of designing a cost-effective alternative to the K_a-band LNA Hybrid, for frequencies between 27 GHz and 31 GHz while adhering to the performance specifications detailed in Table 1.2. To achieve this, various design options were evaluated which included the use of COTS components, commercial PCB materials, and different design strategies aimed at achieving a system better suited for high-volume production.

From this, we also aimed to establish a recommended approach for designing similar systems. Said design approach will cover the fundamental theory that goes into LNA system design and what tools and design steps may be taken. It will also provide suggestions on how to compare different design options, such as substrate materials, components, and system configurations, based on their cost and suitability for the harsh operating environment.

Table 1.2: Relevant Parameter Performance Specifications based on K_a-band Hybrid LNA

Parameter	**Desired Perf.**	**Required Perf.**
Amplitude linearity (OIP3) (dBm)	> 20	18
Gain (dB)	40 to 55	40 to 50
Noise figure, 23°C amb. (dB)	< 1.8	≤ 2
Power consumption (W)	< 0.73	0.75
Input Return loss (dB)	> 20	20
Output Return loss (dB)	> 16	16

Through the adopted design approach and the developed system implementation, this report aims to address the following research questions:

1. How does a low-cost alternative of an LNA system for LEO satellites compare to the current Hi-Rel implementation in terms of performance?
2. What design strategies can be utilised to reduce the overall cost of an LNA system?
3. What qualities and characteristics must a design option possess to be deemed suitable for use in an LNA system intended for LEO satellites?
4. What are the trade-offs between cost and performance when designing an LNA system intended for high-volume satellite constellations in LEO?
5. What industry-related challenges may hinder the full adoption of the New Space paradigm in the design and development of LNA systems?

1.6 Delimitations

This project limited itself to investigating and presenting design alternatives only for the K_a-band LNA Hybrid amplifier chain. In other words, no investigations was done concerning the power supply, gain control system or the interconnection to the system chassis. The design was based around the K_a-band, specifically 27 to 31 GHz, and assumed that an interface with the WR28 waveguides was already established. Although not all frequencies are utilised in commercial satellite systems, we chose to replicate the Hi-Rel system in its entirety to explore the potential challenges and limitations involved in developing a low-cost alternative.

Regarding evaluating system performance, the project limited its assessment to the following parameters: power consumption (excluding DC/DC converter), noise figure, gain, amplitude linearity (OIP3) and return loss (RL). Two other performance metrics, which are usually considered during the design of LNA systems, are gain flatness and stability. Gain flatness describes how uniform the gain is over the specified frequency band and, together with gain stability, should ideally be $< 1\,\mathrm{dBpp}$. Neither gain flatness nor stability was included in the performance goals of the LNA system design. Later sections of this report explains how limited access to data on the components used forced us to prioritise optimising the system for its most significant metrics.

As previously stated in this chapter, all satellite applications must fulfil many requirements when it comes to system reliability to be able to operate within the harsh environment of space. This means that, while primarily focusing on evaluating commercial components and materials against performance specifications, the design also had to address key environmental concerns. As discussed in Section 1.2, a COTS component's ability to withstand radiation is an important aspect which cannot be ignored and thus had to be considered during the selection of suitable components. The ability to withstand vibrations and shocks is another critical challenge in space applications, particularly due to the intense mechanical stress they experience when launched. However, for this particular application, most of the appropriate measures are mechanical solutions performed on the chassis and/or the connection between the board and the chassis, which is outside of the scope of this project. After discussions with advisors at Beyond Gravity, concerns regarding outgassing from component packaging are deemed irrelevant as well, as outgassing poses no risks towards this particular system's functionality.

Since the purpose is to implement a system which is both commercially available and manufacturable, we had to conform to certain design restrictions set on us by our PCB supplier, Cogra Pro AB (www.cogra.se). Cogra only had a limited selection of substrates, so we could not freely choose any arbitrary substrate from specific suppliers. Instead, we limited ourselves to the substrates readily available at the time the project was carried out. The same was true regarding the minimum dimensional restrictions, which could not be smaller than what was possible to manufacture. These restrictions consider both substrate and copper thickness, as well as conductor width, hole diameter, annular ring and conductor isolation.

The final system implementations was not manufactured and put through a comprehensive measurement and testing procedure to abide by the project timeline. However, this report outlines the design process regarding an evaluation board containing key segments of the system chains, as to highlight what challenges and constraints influenced its design.

The performed cost-analysis, to be detailed in Chapter 3, did not take into account the cost of designing and manufacturing the stencil, which is required for the assembly line to manufacture the PCB, nor the chassis or any other support encasing the system. Neither did it take into account the potential cost in terms of screening and testing the system alternatives' sufficiency in terms of reliability.

1.7 Thesis Outline

After the introduction, which outlines the background and motivation of this thesis, the report presents the relevant theoretical framework essential for understanding the project. This will introduce the fundamentals for designing systems operating with radio frequency (RF) signal. It includes essential RF theory, e.g. transmission lines and scattering parameters, as well as some specific terminology associated with RF system design, e.g. noise figure and filter design. Chapter 2 also outlines the relevant material concepts which were considered when designing our system. This includes the introduction of material-dependent parameters which influence the system's performance and environmental resilience, alongside an overview of specific substrate categories considered for our system alternatives.

Chapter 3 introduces the methods used for achieving the goals and purpose of the project. It explains how data for the study was gathered, the design and simulation tools used, and the guiding philosophy behind our design approach. Chapter 3 then transitions into the exploration of the system alternatives and details the process of designing and evaluating a low-cost implementation of the K_a-band LNA Hybrid. Our system exploration is divided into phases, which correspond to the phases of the design process in chronological order. Although no measurements or system testing will be carried out, Chapter 4 will also outline the evaluation board's design process. This is to highlight the challenges and constraints that influence its development. While not directly connected to the thesis' research questions, the development of the evaluation board has a significant role in the future work and studies surrounding the to-be detailed system implementations.

After a sufficient exploration of the design alternatives encountered during this thesis, the final implemented designs are presented in the Chapter 5. This chapter provides a detailed description of the final low-cost systems and outlines the impact of the most significant design decisions. Lastly, the thesis leaves off with a discussion and conclusion surrounding the final design implementations and the research questions investigated throughout this project. It brings up how design decisions and constraints influenced the final results, what could be improved for the future and the challenges within the industry.

2

Theory

This chapter is intended to equip readers with the foundational knowledge required to grasp the intricacies of RF design. The content is primarily tailored for readers with a background in digital systems and embedded design, as many of the concepts may already be familiar to those experienced in microwave engineering.

RF signals usually refer to alternating current signals with high frequencies, ranging from 100 MHz to 1 THz [22]. This corresponds to an electromagnetic (EM) wavelength λ, ranging approximately from 3 m to 300 µm. In both literature and many research papers, the terms RF and microwave frequencies are often used interchangeably. While RF is fairly well defined, microwave frequencies are not as definitive. In David M. Pozar's book *Microwave Engineering* [22], which is highly credited by many researchers in the field, microwaves are referred to as frequencies spanning between 3 GHz to 300 GHz. However, researchers in recent years have advocated towards splitting this spectrum into separate categories where frequencies between 30 GHz and 300 GHz are denoted as *millimetre waves* [23]. The frequency band for which our intended LNA is designed, the K_a-band, corresponds to a frequency range of 27 GHz to 40 GHz, right on the edge between microwave and millimetre wave. This means that the relevant theory highlighted in this report will draw from principles related to RF, microwaves and millimetre waves, and thus these terms will be used interchangeably.

The chapter starts by outlining the fundamental theory behind designing and realising transmission lines and how signal reflection can be minimised by impedance matching. It covers many of the topics and equations which our system design tool utilises and is based upon. This is followed by theory covering important design parameters used to characterise RF devices such as LNAs and passives. Also included is relevant theory on how transmission lines can be designed to create signal filters and signal isolators. This chapter also presents essential theory related to the circuit board materials evaluated and used in the project. In particular, it outlines different material options and the key material parameters that influence RF system performance. Furthermore, the chapter details how the choice of semiconductor material can enhance the radiation tolerance of electronic components.

2.1 Transmission Lines

In traditional traditional circuit analysis, a *transmission line* does not assume that the electrical components are much physically smaller than the electrical wavelength [22], [24]. As a result, currents and voltages vary in amplitude and phase along the transmission line, forming what is known as a *distributed parameter network*, in contrast to the *lumped element network* used in traditional circuit analysis. In other words, the signal's electrical transmission through a conductor cannot be ignored when designing transmission lines.

For transverse electromagnetic (TEM) wave propagation, a transmission line always consists of at least two conductors. It is therefore usually depicted as a two-wire line, as seen in Figure 2.1(a). A section of the transmission line with length dz, can be modelled as a lumped element circuit, presented in Figure 2.1b.

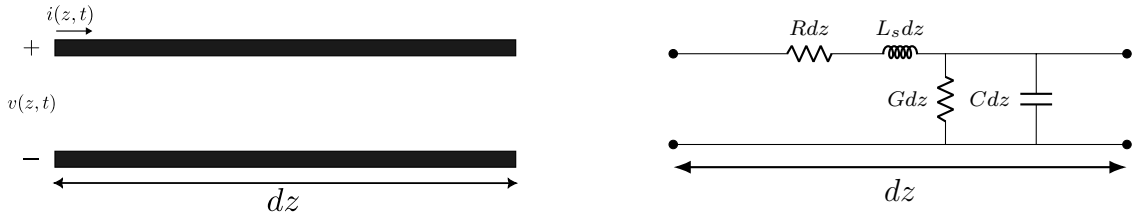

(a) Distributed parameter network **(b)** Lumped circuit model

Figure 2.1: Visual representation of a transmission line as a distributed parameter network and its approximative lumped circuit model.

In Figure 2.1(b), R represents the series resistance of the non-ideal conductor in Ω/m, and L_s is the self-inductance per unit length of both conductors in H/m [22]. The shunt conductance (G, in S/m) comes as a result of the dielectric loss between the conductors while the capacitance per unit length (C, in F/m) is due to the conductors being close to each other.

Assuming a sinusoidal steady-state condition with cosine-based phasors, expressions for the voltage and current propagating through the transmission line can be obtained based on the parameters R, L_s, C and G. These expressions characterise the voltage and current wave equations, and are given by

$$V(z) = V_0^+ e^{-\gamma z} + V_0^- e^{\gamma z} \tag{2.1}$$

$$I(z) = I_0^+ e^{-\gamma z} + I_0^- e^{\gamma z}, \tag{2.2}$$

where γ is the complex propagation constant given by

$$\gamma = \sqrt{(R + j\omega L_s)(G + j\omega C)}. \tag{2.3}$$

$V_0^\pm$ are voltage amplitudes and $I_0^\pm$ are current amplitudes, $e^{-\gamma z}$ represents wave propagation in the positive ($+z$) direction, while $e^{\gamma z}$ represents wave propagation in the negative ($-z$) direction. With (2.1) and (2.2), the *characteristic impedance* of a transmission line can be defined as follows:

$$Z_0 = \sqrt{\frac{R + j\omega L}{G + j\omega C}} = \frac{V_0^+}{I_0^+} = \frac{-V_0^-}{I_0^-}. \tag{2.4}$$

The loss of a transmission line is given by R and G, which, if negligible, can be considered equal to zero. This subsequently gives the following expression for a lossless transmission line:

$$Z_0 = \sqrt{\frac{L_s}{C}}. \tag{2.5}$$

2.1.1 Reflection and Impedance Matching

From (2.1) and (2.2), we note that both the voltage and the current include terms representing waves which propagate in the opposite direction from the transmission path. These terms characterise signals reflected from a load due to an *impedance mismatch* with the connected signal source [22], [25]. Such reflections are undesirable, as they reduce the amount of signal power being delivered to the load. A load with impedance Z_L connected to a transmission line with characteristic impedance Z_0 will not reflect any signals if their impedances are matched, i.e $Z_0 = Z_L$. If, however, $Z_0 \neq Z_L$, a reflecting wave with a voltage amplitude V_0^- proportional to the input amplitude V_0^+ will be introduced into the transmission line. V_0^- is given by

$$V_0^- = \left(\frac{Z_L - Z_0}{Z_L + Z_0}\right) V_0^+, \tag{2.6}$$

from which the voltage *reflection coefficient* Γ can be defined as

$$\Gamma = \frac{V_0^-}{V_0^+} = \left(\frac{Z_L - Z_0}{Z_L + Z_0}\right). \tag{2.7}$$

When $\Gamma = 0$, the load- and characteristic impedances are matched, and there is no reflection, while for $\Gamma = 1$, there is total reflection. The reflection coefficient defines the *return loss* (RL) of an RF system which is a measurement of how much power is received by the load. Thus, a higher return loss indicates better performance. The expression for return loss in dB is given by

$$\mathrm{RL} = -20\log(|\Gamma|). \tag{2.8}$$

For no reflection, maximum power is provided to the load, and $\mathrm{RL} \to \infty$, while for total reflection the return loss is 0 dB.

2.1.2 Scattering and Transmission Parameters

To help detail the behaviour of an RF component, scattering (S) parameters are used to provide information about the reflected, transmitted and incident waves [22]. These parameters are frequency-dependent and usually presented in an $N_p \times N_p$ matrix where N_p is the number of ports in the system. In a two-port system, the S-parameters are given by

$$\mathbf{S} = \begin{bmatrix} S_{11} & S_{12} \\ S_{21} & S_{22} \end{bmatrix}. \tag{2.9}$$

The S-parameters describe the relation between the amplitude of an incident wave V_n^+ to port n and the reflected wave V_n^- from port n. The said relationship for a

two-port system is given by

$$\begin{bmatrix} V_1^- \\ V_2^- \end{bmatrix} = \begin{bmatrix} S_{11} & S_{12} \\ S_{21} & S_{22} \end{bmatrix} \begin{bmatrix} V_1^+ \\ V_2^+ \end{bmatrix}. \tag{2.10}$$

The S-parameters of a two-port system also have some commonly used nomenclature associated with them. S_{11} and S_{22} correspond to the reflection coefficients at the first and second port respectively, thereby providing a model of how well Z_L is impedance matched to Z_0. The return loss at each port is given by (2.8) according to

$$\mathrm{RL}_1 = -20\log(|S_{11}|) \tag{2.11}$$

and

$$\mathrm{RL}_2 = -20\log(|S_{22}|). \tag{2.12}$$

The S_{21} parameter corresponds to the transmission coefficient from the first port to the second port, i.e. the *gain* (active device) or *insertion loss* (passive device) of the system. In the reverse direction, the S_{12} parameter describes how effectively the system isolates signals propagating backward. The system is only considered isolated when $S_{12} \approx 0$. For a two-port system, the transmission parameters can be defined by the $ABCD$ matrix, given by

$$\begin{bmatrix} V_1 \\ I_1 \end{bmatrix} = \begin{bmatrix} A & B \\ C & D \end{bmatrix} \begin{bmatrix} V_2 \\ I_2 \end{bmatrix} \tag{2.13}$$

where V_1 and I_1 are the voltage and current entering the system, V_2 and I_2 are the voltage and current exiting, while $A, B, C,$ and D are the transmission parameters.

2.1.3 Striplines and Microstrip Lines

A useful type of transmission line for RF circuits is the *stripline* [22]. It is a type of waveguide and planar transmission line which consists of a thin conductor surrounded by a dielectric substrate, as illustrated in Figure 2.2(a). The stripline is a conducting strip of width W_s and thickness (sidewall width) t_s, and is centred between two grounded planes. Said planes have a width W_{GND}, where $W_{GND} >> W_s$, and they are placed apart at a distance of d_s. Because of the stripline's structure, with two conductors separated by a homogeneous dielectric with relative permittivity ϵ_r, it can support a TEM wave and, subsequently, an RF signal. It is not, however, all modes of a TEM that are desired, and some higher-order, undesired modes can be mitigated by restricting d_s and t_s to be smaller than $\lambda/2$. Because $d_s > t_s$, the restriction of d_s relative to t_s can be ensured by shorting vias between the two ground planes. Additionally, shorting vias can be used in the transition between a coaxial cable and a stripline, as the transition introduces an asymmetry between the ground planes, which can also induce higher-order modes.

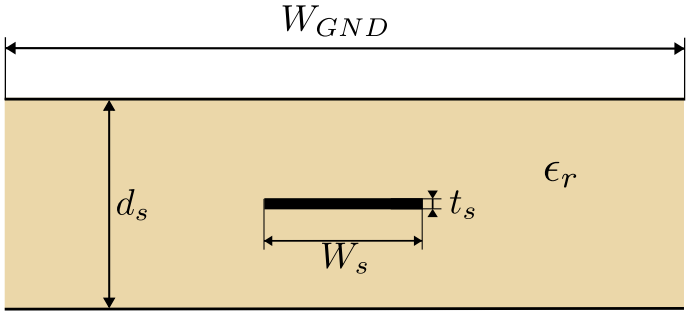

(a) Geometric model of a stripline

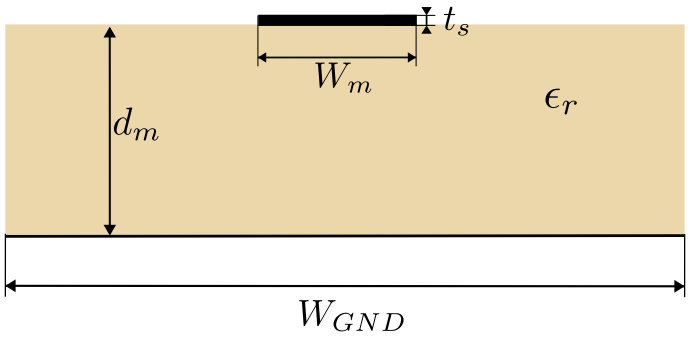

(b) Geometric model of a microstrip line

Figure 2.2: Visualisation of the geometry of striplines and microstrip lines. Illustrations drawn based on images from [22].

The characteristic impedance of the lossless stripline is given by

$$Z_0 = \sqrt{\frac{L_s}{C}} = \frac{\sqrt{\epsilon_r}}{c \cdot C} = \frac{30\pi d_s}{\sqrt{\epsilon_r}(W_{s,\text{eff}} + 0.441d)} \tag{2.14}$$

where c is the speed of light and $W_{s,\text{eff}}$ is the effective width of the strip given by

$$\frac{W_{s,\text{eff}}}{d_s} = \frac{W_s}{d_s} - \begin{cases} (0.35 - \frac{W_s}{d_s})^2 & \text{if } \frac{W_s}{d_s} < 0.35 \\ 0 & \text{if } \frac{W_s}{d_s} > 0.35. \end{cases} \tag{2.15}$$

Given Z_0, d_s and ϵ_r, (2.14) and (2.15) allow calculation of the ratio between W_s and d_s according to

$$\frac{W_s}{d_s} = \begin{cases} x & \text{if } \sqrt{\epsilon_r} Z_0 < 120\,\Omega \\ 0.85 - \sqrt{0.6 - x} & \text{if } \sqrt{\epsilon_r} Z_0 > 120\,\Omega \end{cases} \tag{2.16}$$

where

$$x = \frac{30\pi}{\sqrt{\epsilon_r} Z_0} - 0.441. \tag{2.17}$$

Similar to the stripline is the *microstrip line* [22], [26]. The microstrip line, which has a conductor width of W_m, is placed on top of a thin dielectric substrate with thickness d_m and relative permittivity ϵ_r, as shown in Figure 2.2(b). In contrast

to the stripline, the microstrip line cannot support a pure TEM mode. Instead, a quasi-TEM mode is preferred. In practice, this leads to slightly more complicated expressions for the characteristic impedance of the microstrip line. Said impedance is given by

$$Z_0 = \begin{cases} \frac{60}{\sqrt{\epsilon_e}} \ln\left(\frac{8d_m}{W_m} + \frac{W_m}{4d_m}\right) & \text{if } \frac{W_m}{d_m} \leq 1 \\ \frac{120\pi}{\sqrt{\epsilon_e}\left(\frac{W_m}{d_m} + 1.393 + 0.667 \ln\left(\frac{W_m}{d_m} + 1.444\right)\right)} & \text{if } \frac{W_m}{d_m} \geq 1 \end{cases} \tag{2.18}$$

where ϵ_e is the effective dielectric constant for a microstrip line which is given by

$$\epsilon_e \approx \frac{\epsilon_r + 1}{2} + \frac{\epsilon_r - 1}{2\left(\sqrt{1 + 12\frac{d_m}{W_m}}\right)}. \tag{2.19}$$

Again, from Z_0, ϵ_r and d_m, the conductor width W_m can be calculated according to

$$\frac{W_m}{d_m} = \begin{cases} \frac{8e^{\xi}}{e^{2\xi} - 2} & \text{if } \frac{W_m}{d_m} < 2 \\ \frac{2}{\pi}\left[\beta - 1 - \ln(2\beta - 1) + \frac{\epsilon_r - 1}{2\epsilon_r}\left(\ln(\beta - 1) + 0.39 - \frac{0.61}{\epsilon_r}\right)\right] & \text{if } \frac{W_m}{d_m} > 2 \end{cases} \tag{2.20}$$

where

$$\xi = \frac{Z_0}{60}\sqrt{\frac{\epsilon_r + 1}{2}} + \frac{\epsilon_r - 1}{\epsilon_r + 1}\left(0.23 + \frac{0.11}{\epsilon_r}\right), \quad \beta = \frac{377\pi}{2Z_0\sqrt{\epsilon_r}}. \tag{2.21}$$

2.1.4 Stubs

A stub is a microstrip with an end that is either shorted ($Z_L = 0$) or open ($Z_L \to \infty$) [22], [27]. The stub can either be placed in series (Figure 2.3(a)) or shunt (Figure 2.3(b)) and has different properties depending on length l and characteristic impedance Z_0, which in turn is heavily dependent on the stub's width w_s.

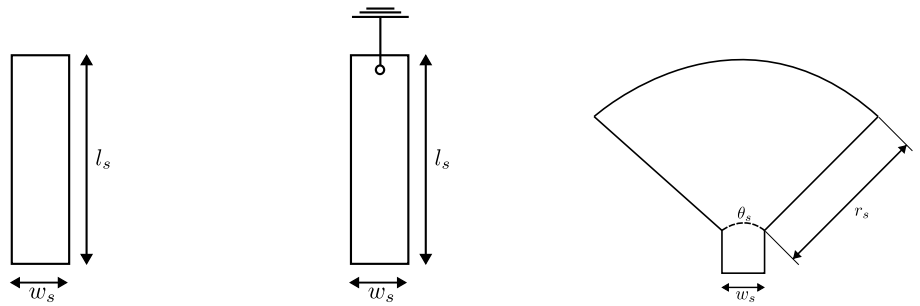

(a) Series Stub **(b)** Shunt Stub **(c)** Radial Stub

Figure 2.3: Combined geometry of open, shunt, and radial stubs.

An open microstrip stub of length $\lambda/4$ can often be used to establish a short-circuit to ground for signals at high frequencies, while allowing low frequencies, such as DC signals, to pass through [27]. This provides the possibility to conduct DC signals while isolating RF, allowing for the bias voltage of an active component to be

provided. Alternatively, these stubs can also be used to create an artificial ground over a specific frequency range. This is particularly beneficial in system designs where the distance between the RF and ground planes is too large for effective signal transmission. *Radial stubs*, a category of open stubs presented in Figure 2.3(c), are especially effective for this particular purpose as they provide extremely low impedance over a broad frequency range.

2.2 Noise Figure

In microwave systems, noise has the undesired effect of limiting the minimal detectable signal strength of the system [22]. Noise can enter the system from external sources, such as cosmic background radiation and stellar noise, but it can also be generated internally within the system's components themselves. The *noise figure* (F) is used to quantify the overall impact of noise in a microwave system and is often one of its most important performance parameters. Specifically, it defines the degradation of the signal-to-noise ratio (SNR) from the input to the output of a component, such as an amplifier [22] [28]. F is subsequently given by

$$F = \frac{\mathrm{SNR}_{in}}{\mathrm{SNR}_{out}} \geq 1. \tag{2.22}$$

Therefore, the noise figure in a system should be as close to unity as possible, corresponding to no further degradation of the signal power due to noise interference. The noise figure of a cascaded system (F_c) is given by

$$F_c = F_1 + \frac{F_2 - 1}{G_1} + \frac{F_3 - 1}{G_1 G_2} + \ ... \ + \frac{F_n - 1}{G_1 G_2 ... G_{n-1}} \tag{2.23}$$

where F_n is the noise figure for component n and G_n is its gain (or insertion loss) [28]. From (2.23), it is evident that the noise figure of the first stage (F_1) has the greatest impact on F_c. In component datasheets, the noise figure is often specified for a matched input source of $50\,\Omega$, as well as for a noise source equivalent to a matched load at a temperature of $290\,\mathrm{K}$.

For passive lossy components, such as attenuators, it is more common that they are described by their insertion loss L, rather than by a noise figure value. The relation between the insertion loss and noise figure is temperature dependent (T)

$$F = 1 + (L - 1)\frac{T}{T_0}, \tag{2.24}$$

and at around $290\,\mathrm{K}$ (T_0) they are equivalent to one another. The power gain of a passive component G, can also be derived from its insertion loss as follows:

$$L = \frac{1}{G} > 1 \tag{2.25}$$

This implies that the total cascaded gain of a system, calculated as the sum of all individual gains and insertion losses, decreases when more passive components are inserted.

2.3 Harmonic and Intermodulation Distortion

No component is truly linear or deterministic across an unlimited range of input and output signal levels, especially for amplifiers operating at high signal power [22]. Under these conditions, the amplifier's performance may be significantly impacted by distortion. This distortion is a result of the existence of other frequency components which may fall within the passband of the amplifier. One particular category of frequency components is *harmonics*, which are multiples of the fundamental frequencies used in the system.

For a single input sine wave, these components typically fall outside the passband. However, things get more challenging as we consider input signals that are made up of two frequencies which are closely spaced together. Alongside their respective harmonics, they also introduce so-called *intermodulation products* which are frequency components of a particular order that are a combination of the two values. Table 2.1 lists the frequency components for both the *second-order products* and the *third-order products*. While all these components are undesirable in the amplifier, the majority can be easily filtered out. The intermodulation products that are of the biggest concern are the third-order's two difference terms, $2\omega_1 - \omega_2$ and $2\omega_2 - \omega_1$. These two products are found present near the two fundamental frequencies and are thus at risk of distorting the output signal. This is referred to as *third-order intermodulation distortion*.

Table 2.1: Frequency components for the second-order products and the third-order products. These are combinations of the two angular input frequencies ω_1 and ω_2.

Second-Order Products	**Third-Order Products**
$2\omega_1$	$3\omega_1$
$2\omega_2$	$3\omega_2$
$\omega_1 + \omega_2$	$2\omega_1 + \omega_2$
$\omega_1 - \omega_2$	$2\omega_2 + \omega_1$
	$2\omega_1 - \omega_2$
	$2\omega_2 - \omega_1$

2.3.1 Third-Order Intercept Point

The *third-order intercept point* (IP3) is a performance metric used to describe the linearity of RF and microwave devices such as amplifiers [17]. As shown in Figure 2.4, it is the theoretical point on a linear power scale where the signal power from third-order intermodulation products intercepts the base signals. In reality, the output power of a device often stops its linear behaviour before reaching this theoretical value and instead saturates. Often it is the IP3 value at the output of an amplifier (OIP3) that is used to assess its resistance against intermodulation distortion. A device with a high OIP3 allows for higher signal powers before distortion is at risk of being generated. In the case where the contributions of intermodulation products are coherent, which is the same as saying that they are very close to the fundamental

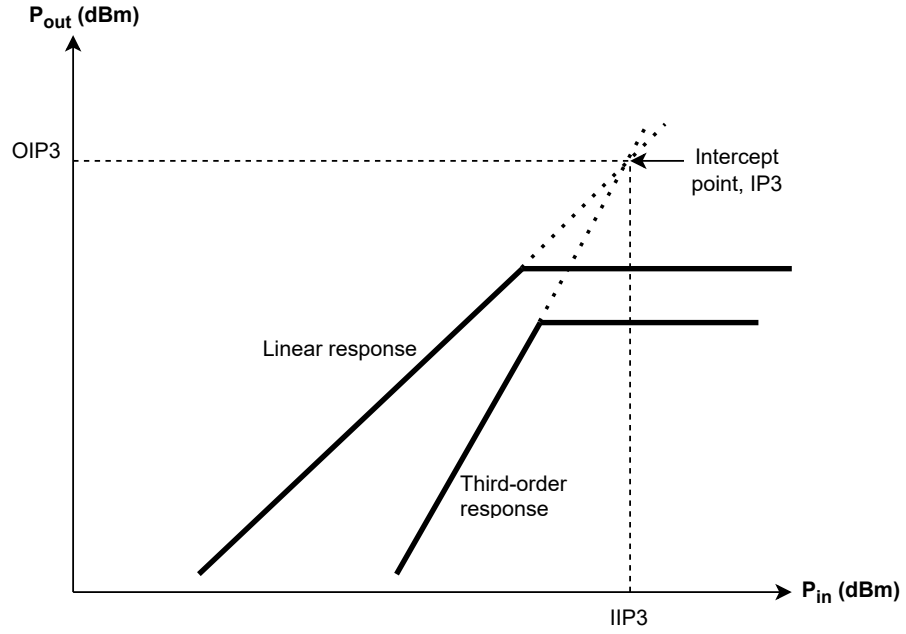

Figure 2.4: Third-order intercept diagram for nonlinear devices [17].

signals, the OIP3 of a cascaded system may be calculated using (2.26) [17]. For a cascaded system of two components, OIP3′ represents the first stage and the second stage is represented by OIP3″. Additional stages may be calculated by letting OIP3′ represent the equivalent intercept point of the prior stages and OIP3″ then denotes the added stage.

$$\mathrm{OIP3} = \left(\frac{1}{G'' \cdot \mathrm{OIP3}'} + \frac{1}{\mathrm{OIP3}''}\right)^{-1} \tag{2.26}$$

2.4 Filter Design using Distributed Elements

A passive component is a distributed element when the wavelength λ of the signal is comparable to the component size [29]. When the RF component length l is much smaller than the wavelength, typically $l < \lambda/20$, the component is considered lumped. Lumped components do not experience significant phase variations over the element, while distributed elements do. Distributed elements are therefore usually characterised by their length l and characteristic impedance Z_0. A lumped model of a BP filter, such as the one presented in Figure 2.5, is not feasible when designing for micro- or millimetre waves where the wavelength is $\sim 1\,\mathrm{cm}$ [26]. High frequencies, therefore, imply the necessity of using distributed components for the implementation of a signal filter.

2.4.1 Parallel-coupled Line Bandpass Filter

A commonly used implementation of the BP filter through distributed components is the parallel-coupled line (PCL) BP filter [26]. This type of filter offers great

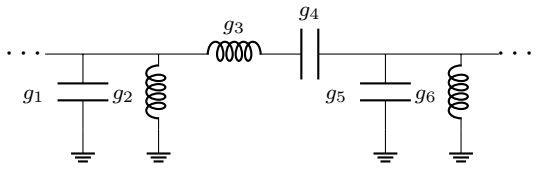

Figure 2.5: BP filter model using lumped components [25], [26].

performance in terms of its possible bandpass specifications, being as narrow as 1% of the centre frequency, and as wide as 40%. The filter design utilises microstrips to form resonators, which are coupled in pairs by placing them in close proximity to one another. In the case of *interdigitated filters*, a subcategory of PCL BP filters (Figure 2.6(a)), coupling is also achieved by shorting one end of the microstrip line. They have the drawback of requiring vias to connect their ground ports, which is often undesired for high-performance filters, as handling a multitude of vias gets unnecessarily tedious for the layout designer. Instead, *edge-coupled filters* (Figure 2.6(b)) are often preferred where intermediate resonators are coupled with two different microstrip lines, creating a stair-like pattern.

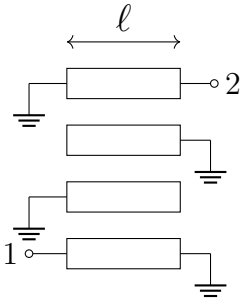

(a) Interdigitated filter configuration

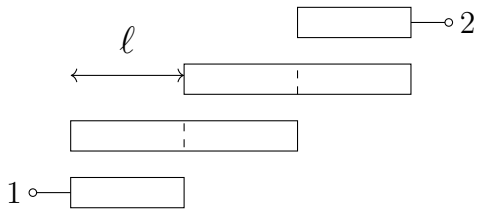

(b) Edge-coupled filter configuration

Figure 2.6: Bandpass filter design configuration using microstrips. Illustrations are based on the designs found in [26].

To calculate the impedances for each resonator cell, (2.27) or (2.28) can be used, depending on whether the impedance order is even (common mode) or odd (differential mode), respectively:

$$Z_{0e} = Z_0 \cdot [1 + JZ_0 + (JZ_0)^2] \tag{2.27}$$

and

$$Z_{0o} = Z_0 \cdot [1 - JZ_0 + (JZ_0)^2], \tag{2.28}$$

where J is the admittance of the resonators. The microstrip lines are, in actuality, designed as admittance inverters, which are two-port lumped-component networks that invert and scale an admittance. However, when used in microwave systems, they act as resonators. The value of the unitless JZ_0 factor for a resonator cell is dependent on its placement in the chain. For the first cell, the factor J_1Z_0 is given by

$$J_1Z_0 = \sqrt{\frac{\pi\alpha}{2g_1}} \tag{2.29}$$

while the factor for the last cell $J_{N+1}Z_0$ is defined as

$$J_{N+1}Z_0 = \sqrt{\frac{\pi\alpha}{2g_N g_{N+1}}}. \tag{2.30}$$

The parameter N denotes the filter order, not to be mistaken with the number of resonator segments n (where $N = n - 1$), and α is the *fractional bandwidth* of the filter which is given by

$$\alpha = \frac{f_2 - f_1}{f0}. \tag{2.31}$$

To calculate the factor for the intermediate cells $J_N Z_0$, the following equation may be used:

$$J_N Z_0 = \sqrt{\frac{\pi\alpha}{2g_{n-1}g_n}} \tag{2.32}$$

By obtaining the values for either the even or odd impedances for the resonators, we can derive their width and separation. This process consists of extensive steps and complex calculations, and is therefore often handled with the aid of software tools. An important note is that the separation carries a massive impact on the filter's passband. The narrower the distance between the two resonators, the broader the passband becomes [30].

2.4.2 Waveguide Stub-Loaded Bandstop Filter

An alternative approach to ensure that only the desired range of frequencies is passed along an RF system is with a bandstop (BS) filter. Figure 2.7 showcases an example of a structure for a BS filter using a *series stub-loaded configuration* with three open stubs [31]. The open stubs represent inductive loads, while the interconnecting loads represent capacitive loads. Together, they correspond to the lumped circuit used to realise the desired BS filter.

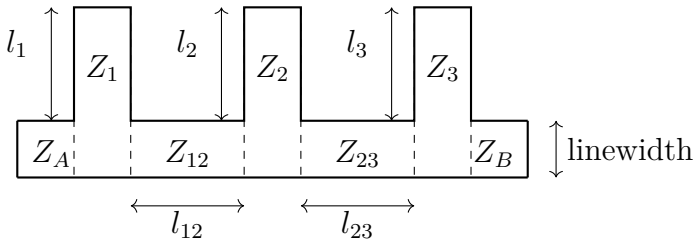

Figure 2.7: Series stub-loaded configuration of a waveguide BS filter using three open stubs of individual lengths (l). Illustration based on designs presented in [32] and [31].

With terminated loads connected to the input (Z_A) and the output (Z_B) of the filter, the individual impedances of the three-step configuration can be calculated as follows:

$$\begin{aligned} Z_1 &= Z_A\left(1 + \frac{1}{\alpha g_0 g_1}\right), \quad Z_{12} = Z_A\left(1 + \alpha g_0 g_1\right), \quad Z_2 = \frac{Z_A g_0}{\alpha g_2}, \\ Z_{23} &= \frac{Z_A g_0}{\alpha g_4}\left(1 + \alpha g_3 g_4\right), \quad Z_3 = \frac{Z_A g_0}{\alpha g_2}\left(1 + \frac{1}{\alpha g_3 g_4}\right). \end{aligned} \tag{2.33}$$

In (2.33), g_i $\{g_i \mid i = 0, \ldots, n\}$ are obtained from the lumped-model circuit of the BS filter, presented in Figure 2.8, and α is the fractional bandwidth given by

$$\alpha = \frac{f_2}{f_0} - \frac{f_0}{f_1}. \tag{2.34}$$

In this case, f_0, f_1, and f_2 correspond to the filter frequencies at the midstopband, lower cutoff and higher cutoff, respectively.

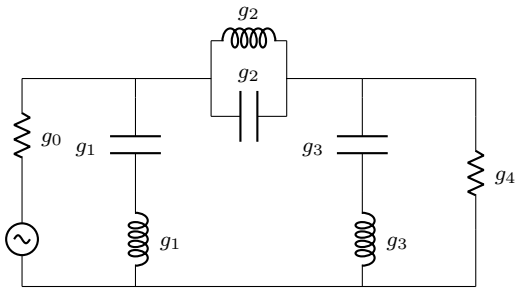

Figure 2.8: Lumped-circuit configuration of three-step BS filter. The drawing is based on illustration found in [25].

2.5 Signal Isolators

Isolators are devices that can be inserted between two RF modules to prevent signals which propagate in the opposite direction from entering the preceding RF module [26]. The isolation of the isolator can be described as the ratio of the input power to the power of the signal propagating in the non-desired direction. For waveguides used within high-power applications, *ferrite isolators* are often utilised. These types of devices provide the benefit of high isolation while maintaining very low insertion loss. The latter is especially important in an LNA system, since it is the earlier stages that carries the most impact on the overall system noise figure. Ferrite isolators are on the other hand very expensive. Fortunately, there are other approaches for realising isolator circuits such as using *quadrature hybrid couplers* (QHC).

2.5.1 Quadrature Hybrid Coupler

The hybrid coupler is a four-port component which splits an input signal into two, half-power signals sent out of two other ports, with no signal propagating through the fourth or the isolated port [22], [26]. There are two types of hybrid couplers: the 180° coupler and the 90° coupler, where the relative phase shift between the output half-power signals is either 180° or ± 90°. A QHC is an 90° hybrid coupler that has the following S-parameters

$$\mathbf{S}_{\text{QHC}} = \frac{1}{\sqrt{2}} \begin{bmatrix} 0 & -j & 1 & 0 \\ -j & 0 & 0 & 1 \\ 1 & 0 & 0 & -j \\ 0 & 1 & -j & 0 \end{bmatrix}, \tag{2.35}$$

where $-j$ corresponds to a $+90°$ phase shift, while j would correspond to a -90° phase shift. At the first input port, the ideal hybrid coupler has zero reflection, i.e. $S_{11} = 0$. The power from the first port to port i is given by $|S_{i1}|^2$, and for the ideal hybrid coupler, zero power exits in the fourth port, meaning $S_{41} = 0$. From the second and third ports, the output signal power is given by $|S_{21}|^2$ and $|S_{31}|^2$, which from (2.35) are given by

$$|S_{21}|^2 = \left(\frac{1}{\sqrt{2}}|j|\right)^2 = \frac{1}{2} \tag{2.36}$$

and

$$|S_{31}|^2 = \left(\frac{1}{\sqrt{2}}|1|\right)^2 = \frac{1}{2}. \tag{2.37}$$

(2.36) and (2.37) show that the input power from the first port is evenly distributed between ports two and three. The signal transmissions from the first port to port i are given by the transmission parameter B_i. At the first port there should be zero reflection, thus $B_1 = 0$. B_2 and B_3 are both $\frac{-j}{\sqrt{2}}$ where both have a half power output but with different phase shifts from the first port (-90° and -180° respectively). Since there should ideally not be an output at the fourth port, $B_4 = 0$. Figure 2.9 presents the geometry of a QHC.

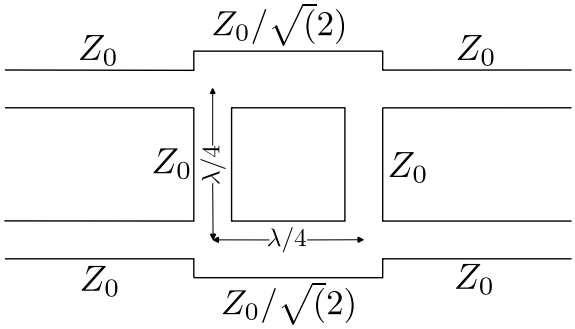

Figure 2.9: Model of an ideal quadrature hybrid coupler.

The quadrature hybrid coupler is a reciprocal device, meaning it can also function as a power combiner when two phase-shifted signals are inserted to the device's two input ports [33]. When the coupler's fourth port is terminated with the source

impedance Z_0 (50 Ω), and both the second and third port are terminated with equal non-Z_0 loads, such as two LNAs, $S_{11} \rightarrow 0$ and the RL at the first port becomes near perfect [33]. This is achieved thanks to the 90° relative phase shift between the output signals from the second and third ports, which results in the reflected waves from said ports dissipating into the fourth one. A second QHC can then be placed after the two non-Z_0 loads, and its power combiner properties allow ideally for an equal signal from the input to the output. The configuration is visualised in Figure 2.10.

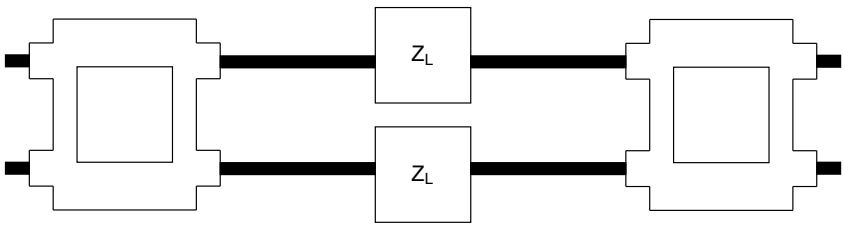

Figure 2.10: Combiner configuration of two QHCs terminated with non-Z_0 loads Z_L.

2.6 Material Properties

In RF system design, various material properties can influence its performance and reliability. For this system implementation, the two most relevant material performance properties are *relative permittivity* and *dissipation factor*, while the selection of chip material is essential to assess the component's resilience against radiation.

2.6.1 Relative Permittivity

The measure of a material's ability to store electric charge is given by the *relative permittivity* ϵ_r [34], or the *dielectric constant* as it is often referred as within the industry. ϵ_r is mainly material dependent but may also vary depending on the frequency and temperature. The actual permittivity ϵ of a material is given by

$$\epsilon = \epsilon_r \epsilon_0 \tag{2.38}$$

where ϵ_0 is the permittivity of vacuum. As highlighted in (2.14) and (2.18), the choice of material and its ϵ_r carry significant impact on the characteristic impedance of both striplines and microstrip lines. In the case of a given Z_0 (e.g. 50 Ω), a higher relative permittivity would result in a lower ratio between conductor width W and distance between ground planes d as according to (2.16) and (2.20). For a constant d, a decreased ratio implies a decreased conductor width, which for a design means requiring smaller stripline and microstrip line widths.

2.6.2 Dissipation Factor

The *dissipation factor* D_f, also known as the *loss tangent* (tan δ), measures the total power loss relative to the voltage and current in a material [34]. It is directly

proportional to the attenuation of a signal due to dielectric loss a_d according to

$$a_d = \frac{k_0 \epsilon_r (\epsilon_e - 1) D_f}{2\sqrt{\epsilon_e}(\epsilon_r - 1)} \tag{2.39}$$

where k_0 is the wave number in free space, and ϵ_e is given by (2.19) [22]. (2.39) directly implies that a lower dissipation factor ensures better preservation of signal integrity, which is particularly critical in satellite systems to ensure that data is reliably received and transmitted.

2.6.3 Gallium Arsenide Chips for Space

Typical high-frequency LNA systems for space applications prefer not to use the metal oxide silicon field effect transistors (MOSFETs), as these are inherently susceptible to the effects of ionization [35]. The reason for this is the oxide, which contributes to the build-up of a positive charge that decreases the threshold voltage of the transistor. Ionising radiation speeds up the recombination of holes and electrons in the oxide, lowering the threshold voltage. This effect of radiation on MOSFETs has led to other semiconductor materials than Si being preferred in space applications.

One common substitute is GaAs which is a III-V semiconductor known for its strong resistance to radiation-induced degradation [36]. For a heavily doped GaAs field effect transistor, the degradation of the device is minimal up to a total ionising dose of $\sim 10^7$ rad, corresponding to an energy deposition of 100 J/g in GaAs material. This is a substantial difference in comparison to MOSFETs, whose threshold voltage V_T can shift by several volts at a total ionising dose of 10^6 rad, whereas the V_T of GaAs FETs would change by only a few millivolts.

When designing MMICs for high-frequency space applications, the transistors used are usually GaAs high electron mobility transistors (HEMTs) [37]. Their low-noise properties make the GaAs HEMTs useful for fabricating LNAs [38]. The behaviour of a GaAs HEMT is temperature dependent [39]. Specifically, the intrinsic transconductance decreases with increasing temperature, which in turn, also decreases the transistor's gain (S_{21}) while increasing the noise figure (F). For space applications subject to large temperature variations, these fluctuations can have a notable impact on the performance of S_{21} and F of GaAs MMICs.

2.7 Printed Circuit Board Substrates

The substrate which makes up the printed circuit board (PCB) can often be categorised depending on its composition: either organic, inorganic or a combination of the two [40]. Usually, the substrate includes a conductor and an insulator [41]. The conductor is usually copper, with high electrical conductivity and low cost, while the insulator can be explicitly chosen depending on the application of the PCB.

Organic substrates usually have low relative permittivity ϵ_r and a low cost while being simple to manufacture [40]. They also come in a myriad of versions, including, but not limited to, epoxy glass (e.g. flame retardant 4, FR4), epoxy (e.g.

Bismaleimide-Triazine, BT) and cyanate. FR4 is the most common substrate used for PCBs today. It is based on epoxy resin and fibreglass [41], which is cost-effective with an acceptable heat resistance, dimensional stability, good adhesion and suitable for large-scale production.

An inorganic substrate can be composed of materials like metal, glass or silicon, but typical for PCBs is the ceramic substrate [40]. The ceramic substrate's main selling point is its heat resistance, along with increased thermal conductivity. Al_2O_3, commonly known as alumina, is a widely used ceramic substrate [40], [42]. It offers a high relative permittivity of ~ 10 [40] which allows for conductor widths as narrow as 30 µm [43]. Additionally, alumina also offers low dissipation factor, however, it is considerably more expensive than organic substrate materials.

3

Methods

This chapter details the general methods used throughout this research and development project. First, the literature study and data collection is introduced which is then followed by detailed procedure of how the component search was conducted. Afterwards, the general design approach and philosophy are presented. It explains the guiding framework that was followed throughout the development of the system design, especially when decisions had to be made regarding how to proceed with different design options, challenges and constraints.

3.1 Literature Study and Data Collection

This project was initiated with a literature study. The purpose of the study was to build a substantial foundation in RF circuit design, material properties and the critical considerations of space-oriented design. The said study covered the basic RF concepts like transmission lines and S-parameters. It also included specific theory related to components used in the RF design, such as LNAs and filters, as well as PCB materials, their relevant electrical parameters, and how radiation may affect electronic devices. Following the literature study, the project's initial data collection was carried out.

In the first segment of the data collection, the current system implementation of the K_a-band hybrid LNA was examined to gain an understanding of its design, functionality, and system specifications. Most of the relevant information was sourced from the system's datasheet, as well as the datasheets for its components. This data established a foundation for assessing suitable components for our designs, which in turn shaped the scope of the second phase: the component search.

3.2 Component and Material Search

From the data and information obtained from the current implementation of the system, the fundamental requirements for both MMIC LNAs and attenuators could be established. Since it is the first component in a cascaded system that carries the most weight of the total system noise figure F, it was deemed important to have a sufficient quantity of LNA components with a noise figure $\leq 1.8\,\text{dB}$ to accomplish the desired system goals. Both the gain and the OIP3 of the components had to be on-par or greater than the bare die components (15–25 dB and 15–30 dBm respectively)

and also had to be able to operate within the K_a-band. Additionally, their supply voltage should preferably not be higher than 3 V. In terms of material properties, the die had to be made of GaAs to ensure adequate radiation resilience. The components should also be able to operate within temperature ranges of -40 to 85 °C. While not covering the entire temperature range that may be prevalent in space, it is a range which the team at Beyond Gravity notes to be the most prominent for these system modules. The component search was limited to only encapsulated components, i.e no bare die components were considered. With encapsulated components, the system implementation could be better suited for automated mass production processes such as pick and place assembly and reflow soldering. A more automated mass production process, in turn, offers the potential to reduce the overall production cost and makes the final implementation better suited for high-volume satellite constellations.

The encapsulated attenuators had the same requirements regarding operating range (frequency and temperature) and being a GaAs die. Their insertion loss, L, and dynamic range also had to be on par or, in the case of dynamic range, greater than the ones found in the original implementation. A general requirement for both types of components was that they had to be purchasable, either directly from a manufacturer or from other trusted vendors. In this project, suitable components were searched for on Analog Devices (www.analog.com), MACOM (www.macom.com), Qorvo (www.qorvo.com) and United Monolithic Semiconductors (www.ums-rf.com). These are trusted vendors in the industry known for manufacturing encapsulated components that show potential within space applications.

While most information and data regarding the components were obtainable from the vendors, neither the S-parameter files across varying operating temperatures nor any noise parameter files could be acquired. Ideally, the noise parameter files should include parameter values for the component's noise figure across the intended frequency range, allowing them to be integrated into the design tool for system optimisation. The temperature data files are also essential to assess the electrical characterisation of the components and, as noted by Pignol et al. [18], should be provided for at least three different temperatures. Furthermore, the component footprints suitable for our design tools could not be obtained either. These instead had to be manually designed based on component schematics found in their respective datasheets.

The search for suitable materials for our circuit board started with an initial screening of the available materials found at Cogra, a local PCB supplier and manufacturer. The materials were assessed by their relative permittivity ϵ_r and dissipation factor D_f. Appendix A and Appendix B respectively list the components and materials that were studied and investigated.

3.3 Design Philosophy

In general, to design a low-cost implementation of an LNA system, we first need to assert your system specifications. We have to establish what elements make up your system, their performance metrics and individual contributions to the system behaviour. Then we have to establish what performance metrics are of the highest importance and which segments in the system chain carry the most impact on said metrics. For an LNA system, the noise figure has to be kept as low as possible, which is determined by the first component, while the OIP3 should be relatively high and is mainly influenced by the last component.

These aspects are what make up the foundation of our framework, which we use to analyse different design options and approaches. At the same time, the framework also has to consider what options and approaches may allow for a more cost-effective implementation. Since the expectation is that there will be a trade-off between performance and cost, it was essential to establish not only the system specifications but also the minimum acceptable performance loss to achieve cost reduction. This is represented in Table 1.2 with the distinction of required and desired system performance for the individual metrics. The detailed approach used when designing the system will be introduced in the beginning of the following chapter.

3.4 Design and Simulation Tools

Different software tools have been employed and utilised throughout the entire design workflow. MATLAB was used to simulate all possible combinations of the gathered components and to run calculations of each configuration's total noise figure, gain and OIP3 using the equations covered in Chapter 2. Additional calculations were performed on each configuration's total bias current and total component cost. The MATLAB script was also extended to sort out any design configuration whose calculated parameters were outside of the specification requirements. It was proven to be an essential tool to create and evaluate different design configurations.

Keysight Advanced System Design (ADS) 2019 Update 1.0 [44] was the primary tool used to design both the electrical circuit and the layout of our designs. The strength in the tool lies in its simulation abilities, as it has both a schematic S-parameter simulation and Momentum, an EM simulator [45]. The schematic-level simulation tool served as an effective initial step for assessing system behaviour, as it allowed basic models of microstrip lines to be combined with imported S-parameter data for the intended components.

The Momentum simulator is used to obtain a more accurate model of passive microstrip line components and interconnections by simulating the physical layout of the design. This incorporates more real-world effects that may influence the system behaviour than what is considered in schematic-level simulations, such as the real-life behaviour of the EM waves.

3.5 Noise Figure and System Cost Analysis

The estimated noise figure for each design alternative was calculated using (2.23) at every 0.5 GHz interval across the intended frequency range. These calculations were performed using a MATLAB script in which the noise figures extracted from the components' datasheets and the gain values from the LNA's S-parameter files were used. For the attenuators and filters, their average insertion loss across the frequency range was used and converted into the corresponding gain (2.25) and noise figure (2.24) for $T = 290\,\mathrm{K}$. As for the implemented QHC (to be discussed in more detail in the following chapter), its S-parameter file was used to extract the insertion loss at each interval frequency.

Additionally, a cost analysis was conducted for each explored system alternative in comparison to the original system implementation. The said analysis assessed the potential cost savings which could be obtained in terms of component and material cost. Said analysis only accounted for the cost of the purchased material utilised and highlighted throughout the project. Since the finalised system implementation was not manufactured, the factual cost of the circuit board material required could not be determined. Instead, it was assumed to be twice the quoted price for manufacturing the evaluation board. As will be showcased later in the next chapter, half of the final system implementation was segmented onto an evaluation board. We therefore argue that doubling the cost for the entire system was considered a reasonable assumption. Overall, the result from the analysis will only provide a relative comparison in terms of cost-saving potential, as the actual cost of the original system cannot be disclosed.

4

Design Exploration of System Implementations

Before work began on the system design, we analysed the current implementation to identify key areas where costs could be reduced, outlined the necessary design steps to be taken and determined what major design challenges existed. As already discussed throughout this report, using encapsulated COTS components and commercial PCB materials is one efficient approach to reducing cost. However, as noted in the system specifications, one of the more expensive parts of the existing implementation is the WR28 waveguide isolators. This motivated us to also explore design strategies which replaced the isolators with QHC configurations. As mentioned in Section 2.5.1, a QHC can ideally exhibit near-perfect RL at its ports and can be used both as a power splitter and combiner. Furthermore, since it can be implemented using only microstrip lines, it offered a significantly more cost-effective alternative to the complex isolator components. We sought to create two different design implementations: one which utilises QHC configurations and one design intended to keep the existing WR28 isolators. Although our primary focus was on the first implementation, we considered it important to develop an alternative in case the QHC configuration's insertion loss resulted in an unacceptably high noise figure that outweighed the potential cost savings.

The design process was divided into five key phases: i) First, after concluding the component search, we conducted a screening procedure to evaluate various component configurations based on their performance potential. ii) After that, we carried out an analysis to determine the most suitable PCB material for our implementation. This analysis was based on different QHC designs for each of the promising material candidates. Because the QHC offers a high potential to bring down cost and has a significant impact on overall system performance, the material's influence on the QHC's performance was a great point of comparison. iii) Once the board material was selected, work began on designing the BP filter. iv) This was followed by the design and optimisation of the circuits and layouts for the two system implementations. v) In the final phase, the evaluation board, which contained key segments of the final design intended for testing and measurements, was designed but not manufactured.

The main challenge, however, was how we would accurately assess the impact that our various design options had on the system's overall noise figure, F_{tot}, since we did not have the components' noise parameter files at our disposal. Ideally, such

files contain detailed noise data parameters that can be used in our simulation tools to optimise for a minimal noise figure. Unfortunately, these files were not provided by the vendors for our selected commercial components, and the only available information regarding their noise figure was limited to what was stated in their datasheets. This information, however, cannot be used as an input for the design software. To obtain the necessary noise parameters ourselves, we would require extensive measurements for each component and convert them into a suitable data format for the simulation tools. Before that, however, we would have to design and manufacture different evaluation boards for the components to be mounted upon and connected to our measuring setup. To avoid this time-consuming procedure, we instead chose to develop an alternative design approach aimed at optimising the system for an estimated minimal total noise figure, F_{tot}.

Since it is the initial stage in an RF chain which carries the greatest impact on F_{tot} (2.23), our approach focused on minimising the insertion loss introduced by the QHCs at the input. As will be detailed later in this chapter, achieving low insertion loss, L, for the QHCs across the entire passband proved challenging. This presented two possible design strategies: either design the RF chain for a relatively uniform noise figure across the band, or optimise for a minimal noise figure at a limited segment of the band at the expense of higher noise elsewhere. For the QHC-based implementation, we chose the latter to establish a benchmark for evaluating the potential and limitations of designing a cost-effective implementation. Its optimisation frequency was selected after the configuration screening and corresponded to the frequency at which the LNA in the initial stage exhibited its minimum noise figure. For the non-QHC-based implementation, we decided to optimise its design to ensure a relatively uniform noise figure across the intended frequency range. The remaining sections of this chapter will outline each design phase in more detail and highlight the specific design challenges encountered as well as the key decisions made during each stage.

4.1 Phase 1: Configuration Screening

After concluding the component search and gathering the relevant performance data, the next step was to generate and evaluate different component configurations for the two implementations. The initial configuration, shown in Figure 4.1, was based on the structure of the original K_a-hybrid and was limited to a set of three different commercial components in the system chain. With the aid of the self-developed MATLAB script, each possible component configuration was generated, and its cascaded F_{tot}, OIP3, and gain were calculated using (2.23) and (2.26). For the BP filter, which was to be designed directly into the substrate, the noise figure and insertion loss were assumed to be 2 dB, and its OIP3 were assumed to be 100 dBm. These values were estimations from the team at Beyond Gravity based on their experience with similar designs. In the case of the attenuators, where the OIP3 were not listed in the component datasheets, the OIP3 was assumed to be 100 dBm. This is an arbitrary value which, in turn, carries little significance on the outcome of the calculations.

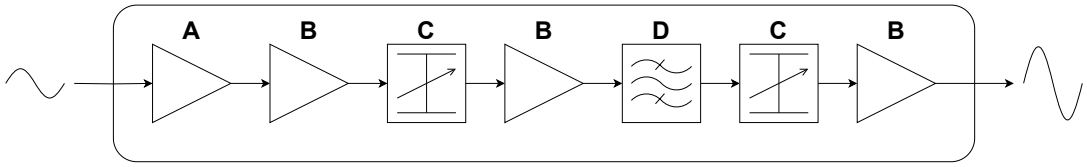

Figure 4.1: The original system set up in its A-B-C-B-D-C-B configuration, where A and B are two different LNAs, C is an attenuator and D the BP filter.

Alongside the cascaded performance parameters, the script also calculated the total component cost and power consumption. The cost was determined as the sum of the market prices of all individual components, while power consumption was calculated as the product of the total average current drawn by the components and the system's supply voltage of 3 V.

Once all configurations were generated and their specifications were calculated, the script then conducted a screening procedure which eliminated any configuration that fell outside of the minimum system requirements. While reviewing the results from the screening procedure (Appendix C.1), it was noted that many configurations with the lowest noise figures and power consumption also exhibited excessively high system gain, reaching values up to 100 dB. Additionally, it was also apparent that the best system noise figure was achieved when using a *MAAL-011238* (MAAL) [46] as the initial LNA of the chain, which had a minimal F of 1.5 dB at 31 GHz. These findings prompted an exploration into an alternative system configuration, shown in Figure 4.2. This includes one fewer LNA and attenuator, which in turn results in an even more cost-effective design better suited for mass production.

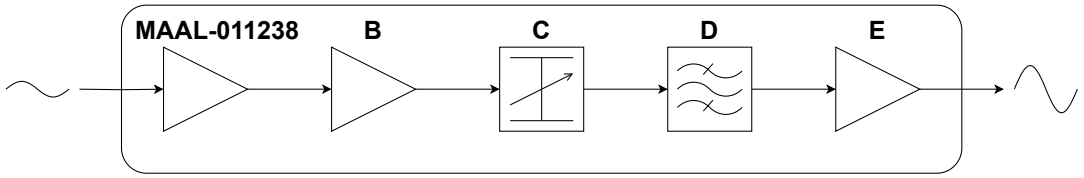

Figure 4.2: Further explored system configuration inspired by the low-gain system presented in Figure 1.2.

The screening script was updated to incorporate the revised configuration structure with a stricter OIP3 threshold to help narrow down the list of candidates. The generated dataset, provided in Appendix C.2, was then manually screened, where we focused on configurations that exhibited the lowest noise figure, highest OIP3, and a system gain that could be adjusted using the attenuator to cover the required range.

At this stage, there are many different factors one may consider when selecting a suitable configuration, such as cost and low power consumption. In our case, we were comparing our implementation to a design which are several magnitudes more expensive. This meant that the difference in cost between the configurations carried little relevance when put in comparison to the hybrid implementation. In terms of power consumption, it was only important for these implementations that

they were aligned with the system requirements. Instead, we choose to eliminate any configurations which include more than two different LNAs. As Pignol et al. remark in their proposed selection procedure [47], it is important to ensure traceability of the entire system. We argue that using a reduced set of components allows for a more streamlined and manageable traceability of our system implementations.

This process resulted in three final configurations, all of which utilised the MAAL LNA for slot B, as well as *HMC519LC4* (HMC) [48] for slot E. In other words, the only distinguishing factor between them was the choice of attenuator. Their respective configuration metrics are listed in Table 4.1. Since all key performance parameters were relatively similar, the most cost-effective option, utilising the *MAAV-011013* (MAAV) [49] attenuator, was selected to be used for our system implementations. One notable remark regarding this configuration is that the selected HMC LNA not only allows for a suitable OIP3 of 23 dBm but also exhibits a sufficient RL of 22 dB at its output to potentially meet the system requirements, without the need for a QHC configuration or a WR28 isolator. This meant that we only needed to design a QHC configuration at the input of the system chain for the QHC-based system implementation.

Table 4.1: Performance metrics for different attenuator choices to be used in the configuration with MAAL-011238 for slots A and B, and HMC519LC4 for slot E.

Attenuator	**Gain (dB)**	F **(dB)**	**OIP3 (dBm)**	**Power (W)**	**Cost (SEK)**
HMC985ALP4KE	71	1.50	23.3	0.375	3640
MAAV-011013	71	1.50	23.2	0.375	3320
MAAT-010521-H1	70	1.50	23.1	0.375	3560

The main takeaways from this design phase were that an efficient script, which is tailored to the designer's interests, was a great tool to identify, assess and narrow down viable component combinations. However, it is important not to take the script's output at face value without certain considerations. For example, certain performance metrics, such as the component's noise figure, vary across frequencies. Therefore, the true behaviour of the configuration across the intended frequency range is best evaluated through dedicated design and simulation tools, and ultimately verified through appropriate testing and measurement procedures.

Another important consideration is how the component's package and biasing network may influence or even hinder certain aspects of the system design. If it were not for the HMC's excellent output RL, the decision to use it within a QHC configuration might have been reconsidered due to its relatively extensive feature size and biasing network. These factors could potentially have challenged the optimisation of the QHC's behaviour and may have led to the selection of a different LNA.

4.2 Phase 2: Substrate Evaluation and QHC Design

After the material search for the circuit board was completed, the options were narrowed down to the four different materials shown in Table 4.2. These materials all have their own distinct qualities and it was of interest to examine how they could potentially influence the design and performance of the system. What was particularly of interest in the analysis was to examine how well the FR4 material fared against the listed Rogers material since it is the most cost-effective of the four. RO3003 and RO3010 were chosen for their low dissipation factor and high permittivity respectively and RO4350B was a common industry material for RF systems according to the team at Beyond Gravity.

Table 4.2: Properties of the PCB materials available to order from Cogra chosen for further investigation.

Material	ϵ_r (10 GHz)	D_f (10 GHz)
FR4 (370HR [50])	3.92	0.0250
Rogers (RO3003 [51])	3.00	0.0010
Rogers (RO3010 [51])	10.20	0.0022
Rogers (RO4350B [52])	3.48	0.0037

As brought up at the beginning of this chapter, the analysis of the different materials was performed by designing a QHC component for each one and then comparing how the choice of material influenced its performance. Since the QHC is the initial segment of the LNA system, it was important to ensure that the choice of material would allow for a microstrip design with both minimal insertion loss and high RL. Before that, however, we had to set up an ideal configuration of the QHC. This was the process for all of our microstrip line components in our system design, as it helped to establish a baseline for evaluating the expected performance behaviour of our non-ideal components. The ideal QHC component was set up as showcased in Figure 4.3. As seen in Figure 4.4, it had a near-perfect return loss at both its input and output. Its power gain was also divided equally between the second and third port for the design frequency, which in this case was 29 GHz, the centre frequency within the intended frequency range. While it may perhaps be more reasonable to base the design around 31 GHz which is the design frequency for the QHC-based implementation, in our assessment of the materials we thought it was important to understand the potential differences that may appear accross the larger set of frequencies. This also helped to assess the materials relevance in future studies where the QHC-based implementation could be optimised for the entire frequency band.

The next step in this phase was to update the transmission lines by replacing the ideal interconnections with material-dependent microstrip lines. This introduced the definition of the substrate, where relative permittivity ϵ_r, dissipation factor D_f, substrate height d_s, conductor thickness t_s and conductor conductivity σ where specified. In the design of all of our microstrip line components, the dimensions d_s and t_s were kept constant and set to be as thin as possible, following the limits of

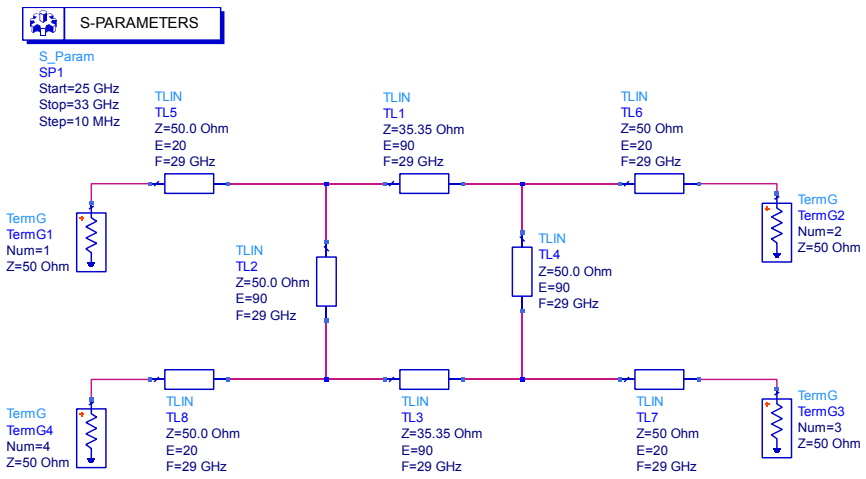

Figure 4.3: Keysight ADS schematic simulation setup of the ideal QHC

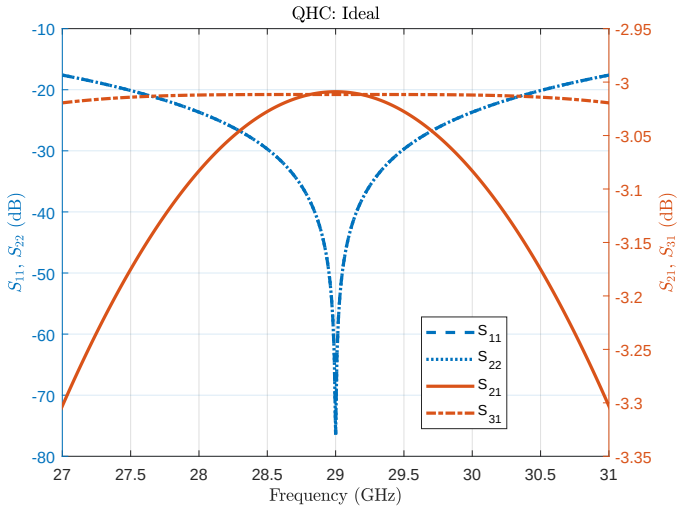

Figure 4.4: S-parameter response from the ideal QHC designed for 29 GHz

the PCB manufacturer's specifications, while the conductivity σ was set to that of copper. The parameter values used, independent of the choice of substrate material, are listed in Table 4.3.

For each QHC design, microstrip dimensions were calculated using Keysight ADS's 'LineCalc' tool, with the material parameters and values in Table 4.3 to match the characteristic impedance of the baseline design. These designs were then individually put through EM optimisation using the EM simulator Momentum. The goal of the EM optimisation was to ensure that the QHC designs behaved as closely to the ideal design as possible, meaning the peak values of S_{21} and S_{31} had to coincide at some frequency between 27 and 31 GHz, at which the RL of the input had to be as high as possible. Preferably, S_{11} had to be low enough to ensure that a majority of the

Table 4.3: Substrate parameters kept constant during simulation of microstrip components.

Substrate Parameter	Value
d_s (mm)	0.2
t_s (μm)	18
σ (S)	$58 \cdot 10^6$

band had an input RL of more than 20 dB, as per the system requirements. The simulation output for each optimised QHC design is shown in Figure 4.5.

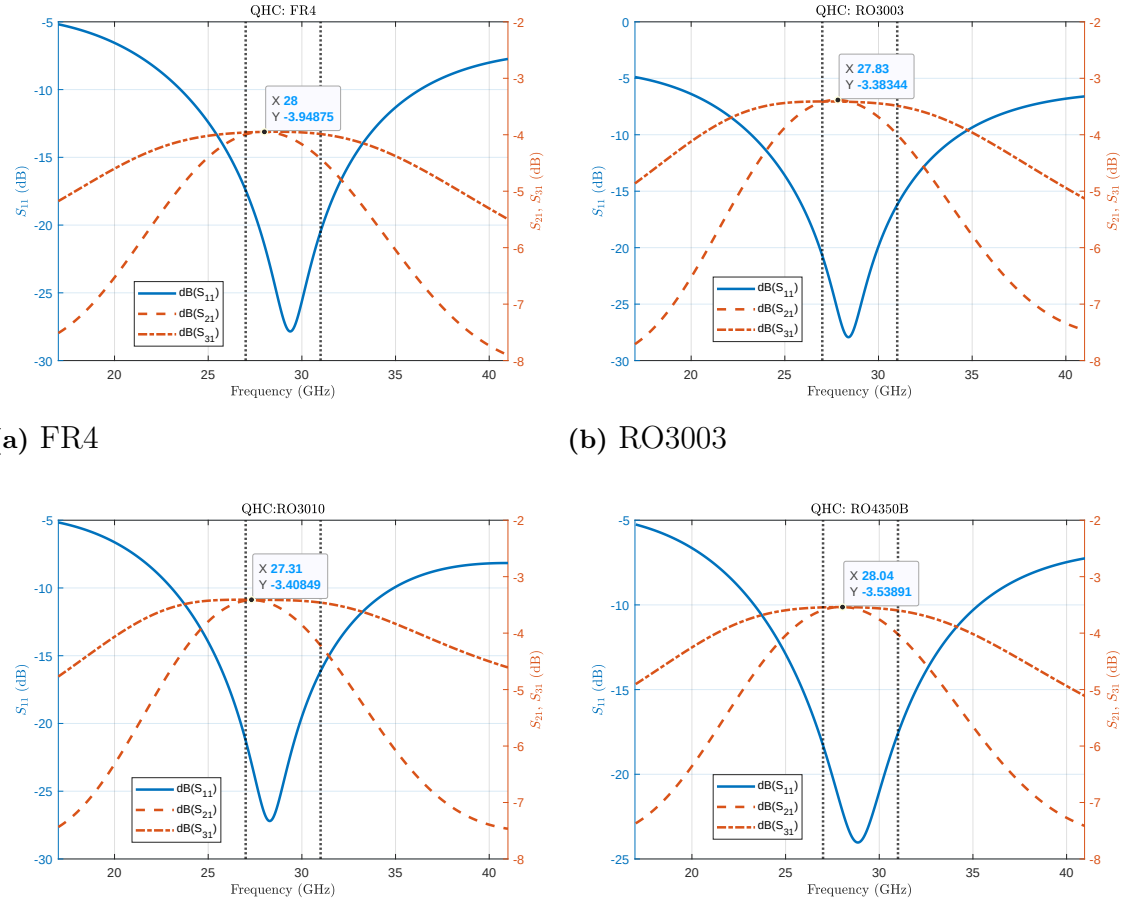

(a) FR4 **(b)** RO3003

(c) RO3010 **(d)** RO4335B

Figure 4.5: Comparison of S_{11}, S_{21} and S_{31} among four QHC configurations based on different substrates.

Our comparison concluded that, aside from the differing levels of insertion loss, the optimised designs behaved relatively similar to eachother, with the FR4 showcasing the highest insertion loss. Out of the four materials, it was the Rogers RO3003 substrate which showcased the lowest insertion loss and thus was deemed most suitable for our system implementation. With the substrate material selected, the RO3003 based QHC design was lastly redesigned to be optimised for 31 GHz.

In this analysis, it is important to note that the choice of substrate material also

influenced the design of the non-QHC implementation. The concept for the non-QHC implementation emerged at a later stage, when concerns were raised regarding the performance of the QHC-based design. Rather than conducting a separate substrate evaluation, we opted to use Rogers RO3003 for both implementations, as it was known to support low-loss interconnections and thus contribute to a minimal estimated noise figure. This decision also allowed us to reuse the same filter design in both implementations, which proved to be time-efficient. Future iterations of this implementation should consider adopting a revised evaluation process to identify the most cost-effective substrate that has minimal impact on overall system performance.

4.3 Phase 3: Filter Design

As with the QHC, the characteristics of the parallel-coupled line (PCL) filter are heavily influenced by the permittivity of the chosen PCB material. Thus, once the choice of PCB material was determined, the design of the PCL BP filter could begin. In Keysight's circuit design layout, a PCL BP filter can be set up using the smart component `DA_CLFilter` and then inserting the corresponding parameter values to obtain the desired behaviour of the filter. For our filter, we used the values listed in Table 4.4.

Table 4.4: Parameter values used for PCL BP filter intended to filter out frequencies outside of 27 to 31 GHz.

Parameter name	Description	Value
Fs1	Lower stopband edge frequency	22 GHz
Fp1	Lower passband edge frequency	27 GHz
Fs2	Upper stopband edge frequency	36 GHz
Fp2	Upper passband edge frequency	31 GHz
N	Number of filter sections	6
Ap	Passband edge attenuation	3 dB
As	Stopband edge attenuation	50 dB

The initial design structure demonstrated promising results, particularly for a fifth-order filter, as shown in Figure 4.6 in regards to attenuating frequencies outside the passband. However, its physical dimensions were too narrow to be reliably manufactured. Some segments of the filter design had a line separation of some tens of micrometres, which is a tenth of the minimal separation which the manufacturer was able to produce. This finding was an early showcase of the potential constraints one may expect when designing a low-cost RF system operating within our passband.

As expected from the relationship between separation and bandwidth, as brought up in Section 2.4.1, our attempts to increase the separation only diminished the quality of the filter. Adjusting the filter order also did not show any improvements. Our initial response to this design challenge was to explore other existing design implementations for BP filters, which were preferably based upon the chosen substrate. In our search, we discovered a published design by D. Sharma and P. Shanti [30], who had developed a microstrip interdigitated filter using Rogers RO3003. This

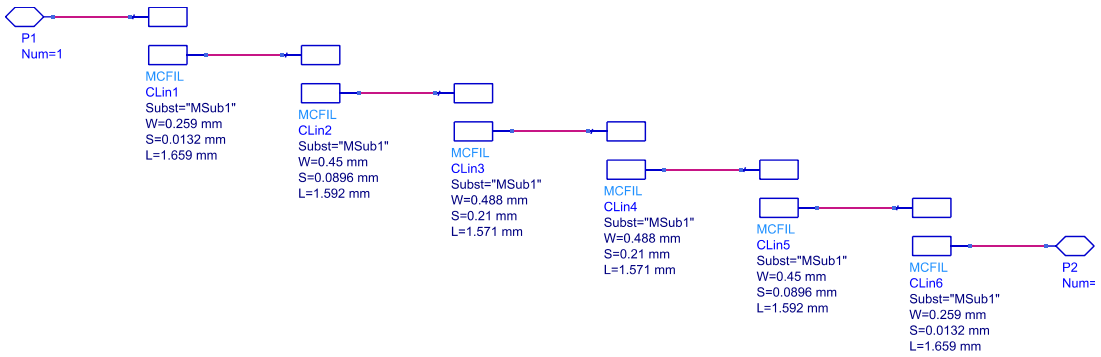

(a) Fifth-order PCL BP filter.

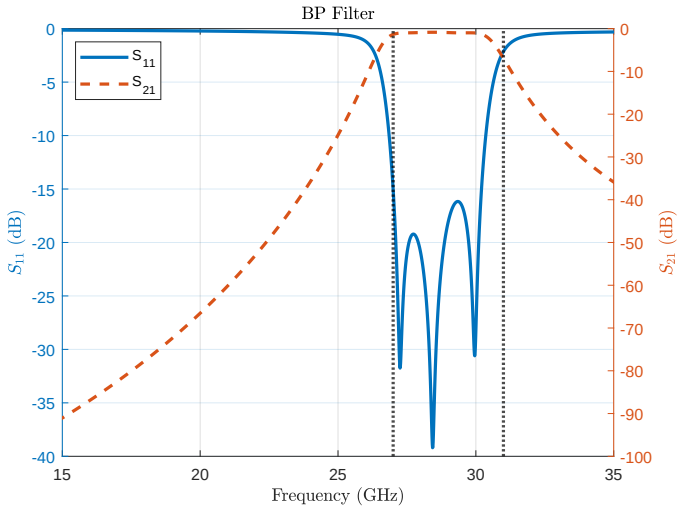

(b) Schematic simulations of configured fifth-order PCL BP filter.

Figure 4.6: Schematic and simulation results of fifth-order PCL BP filter designed around 27 to 31 GHz.

design, although intended for the X-band, also had a bandwidth of 4 GHz in its passband. However, the line separation used, although closer to the requirements than our PCL filter design, was still not sufficient to be manufactured. An alternative approach that was discussed was to use a surface-mounted component for the BP filter. However, the goal of the project was to minimise cost, and we argue it is much more cost-effective to design a filter using copper traces, which outweighs the benefit of purchasing an encapsulated BP filter component.

At this point during the project, we decided to shift our focus towards designing a bandstop filter that could eliminate the signal frequencies that were more prominent to causing issues for the system. In our implementation, the frequencies most important to filter are primarily in the range of 17 to 22 GHz. Fortunately, the WR28 waveguide that is expected to input the RF signal into the LNA system, has a cut-off frequency of 21.1 GHz, which meant we only needed to optimise our filter attenuation for frequencies from the cut-off to 22 GHz. Figure 4.7 shows the circuit design for the initial BS filter, realised using a series-stub-loaded configuration with three open stubs.

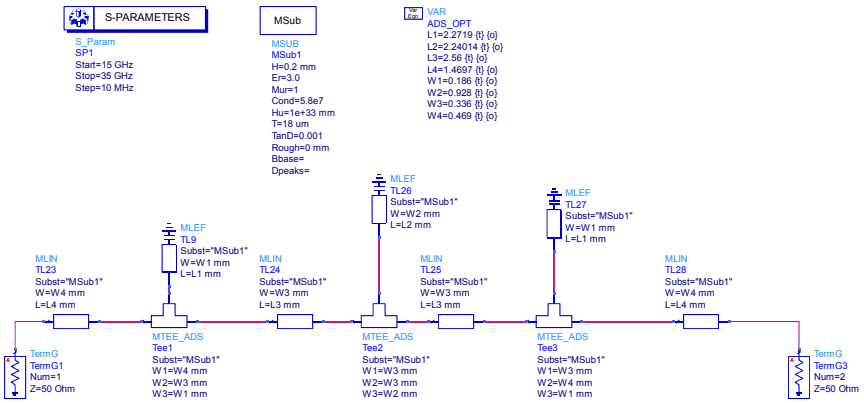

Figure 4.7: Initial circuit design for the BS filter used to filter out frequencies in the range of 21.1 to 22 GHz.

This design was then put through iterative optimisation procedures, with the goals of having 40 dB attenuation in the relevant stopband as well as having less than 0.5 dB ripple in the passband. The final design and its performance are shown in Figure 4.8 and Figure 4.9, respectively. It was important to widen the passband by 1 GHz since the expectation was that, if manufactured, the narrow bandwidth of the realised filter would perhaps attenuate the frequencies at the edges of the passband.

Although sufficient for these system implementations, the key takeaway from this phase is that the use of BP filters in low-cost LNA systems warrants further investigation. In systems where multiple undesired frequency ranges must be attenuated to prevent erroneous behaviour in the receiver, it may not be efficient to incorporate a separate BS filter for each one. Future research could explore the limitations of allowable passband widths when resonator spacing is constrained by manufacturing requirements.

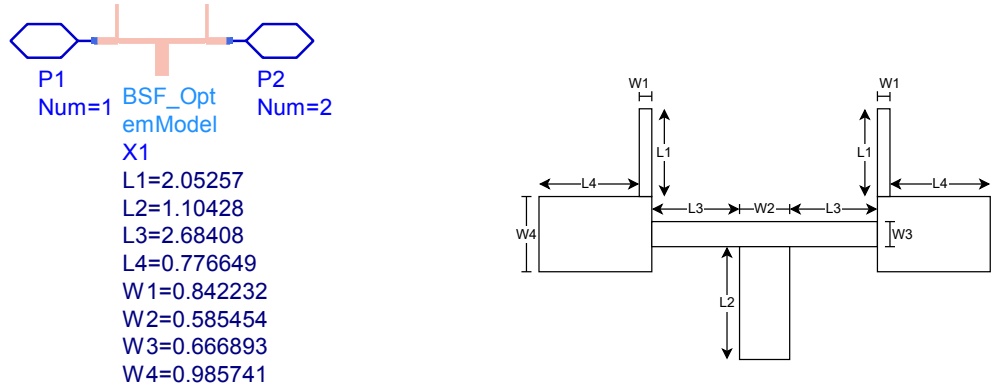

(a) Final BS filter

(b) BS filter dimensions reference.

Figure 4.8: Schematic and simulation results of sixth-order PCL BP filter designed around 27 to 31 GHz.

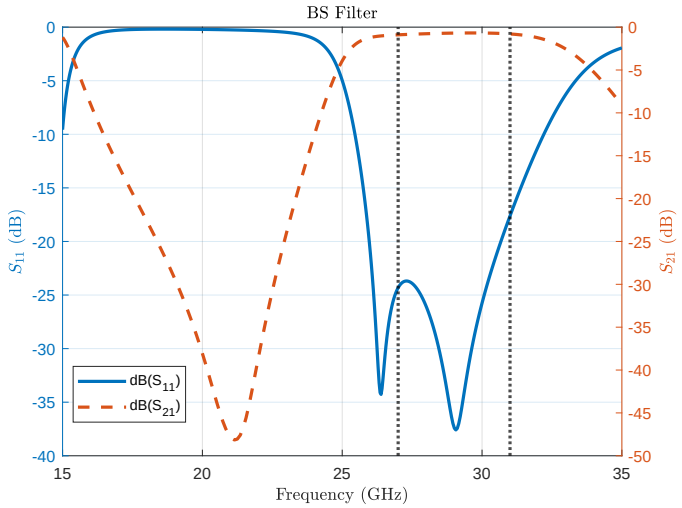

Figure 4.9: Simulation result of filter attenuation (S_{21}) and RL (S_{11}) for the final BS filter design.

4.4 Phase 4: Circuit Design and Optimisation

After the component configuration and substrate material were decided, and the design for the QHC and BS filter was completed, the design of the system chain could commence. The first step was to establish lossless 'ideal' system baselines, which would serve as reference points when optimising the dimensions of the microstrip lines. We chose to have two baseline designs: one which did not incorporate our QHCs (Figure 4.10(a)) and one that did (Figure 4.10(b)), both using cascaded S2P components, which use Touchstone (`.s2p`) files to represent the COTS components' S-parameters. This helped us take note of the impact that our QHC configured as an isolator had on the performance and limitations of the system. As shown in Figure 4.10b, two QHCs were configured in a combiner network with two MAAL LNAs connected in parallel.

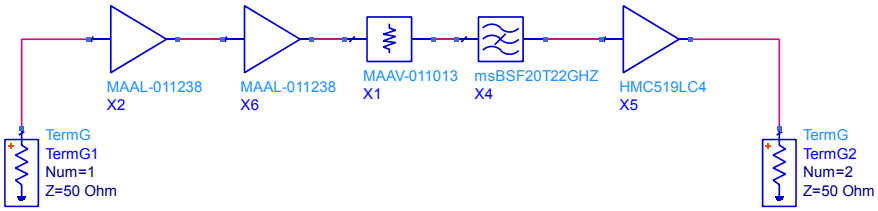

(a) Baseline configuration of RF chain using only S-parameter components and BSF.

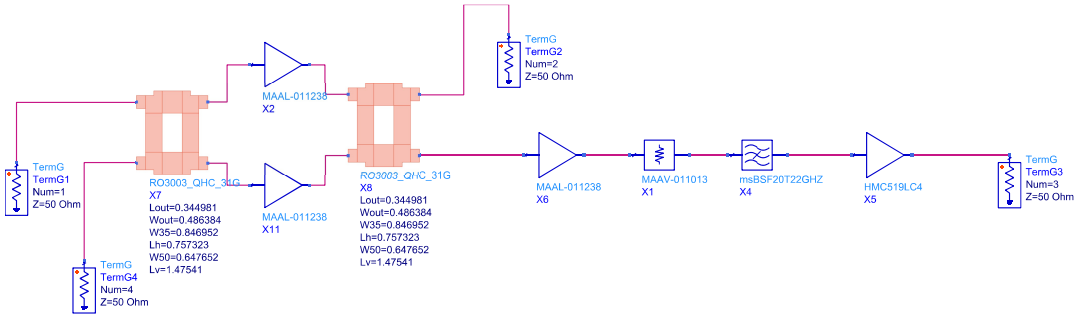

(b) Baseline configuration of RF chain incorporating the QHCs which are designed around 31 GHz.

Figure 4.10: The ideal system configurations used as a baseline for design optimisation.

Afterwards, the circuit design for the QHC-based system implementation was developed, using microstrip line components to interconnect the devices. As with the QHC design, the dimensions of these interconnections were iteratively optimised and tuned to achieve low insertion loss at the design frequency and high RL at both the input and output of the system chain. These files are sometimes provided for

multiple test temperatures. In our design, we were only provided files measured at 290 K, i.e. room temperature.

It is important to note that the circuit design tool treats the S2P components purely as two-port devices. In other words, the simulation output does not consider the influence of the components' other pins or their biasing networks. Thus, the outcome of the circuit design only served as another baseline for our system implementation. Once we transitioned into the layout design, the microstrip lines had to be redrawn to accommodate the components' footprints and biasing networks. They also had to be redrawn to accommodate the minimum allowable line separation and width, per the manufacturer's specifications.

During the layout design of the system, we observed that once the system gain approached 50 dB, the small feature size of the system induced self-oscillation. For a typical LNA system designed at these levels of gain, mechanical solutions are often employed to mitigate this risk. However, since mechanical solutions were outside of the scope of this project, we instead chose to separate the system into two layout segments: one which contained the QHC configuration and one which contained the rest of the system. Once optimised and finalised, these segments could later be generated as standalone components and inserted into a circuit layout. After properly connecting the segments with optimised microstrip lines, the simulation output reflected the intended system behaviour without exhibiting the effects of self-oscillation.

4.4.1 QHC Configuration Optimisation

While everything after the QHC input stage was relatively straightforward to redraw and implement, the QHC configuration posed significant design challenges due to the size of the MAAL LNA package and the constraints imposed by the manufacturer's specifications. As the optimised EM components between the QHCs and the MAALs were very short, we assumed that the best option would be to keep the connections as short as possible to minimise insertion loss, while longitudinally leaving space for supporting passives. The initial result of this design idea is presented in Figure 4.11(a). However, this layout did not yield any satisfactory results. When keeping the interconnections as short as possible, the feature size of the input stage became $\sim 1\,\text{cm}$, which is approximately equal to λ at 31 GHz. This introduced unwanted coupling between the QHCs, which resulted in poor return loss at the input stage.

The solution to this was to separate the two QHCs. Depending on the distance between them, either L could be minimised or RL could be maximised at 31 GHz. We opted to compromise so that the two parameters both remained at acceptable levels, which came as a result of an additional 6 mm between the QHCs. This compromise resulted in a vast improvement in both the input RL and insertion loss for the higher frequencies. The final layout of the input stage is presented in Figure 4.11(b), with its relevant S-parameters presented in Figure 4.12. It is clear from Figure 4.12, that even after the separation of the QHCs, the input RL for the configuration still does not behave quite as expected when compared with, for example, S_{11} of the QHC presented in Figure 4.5b.

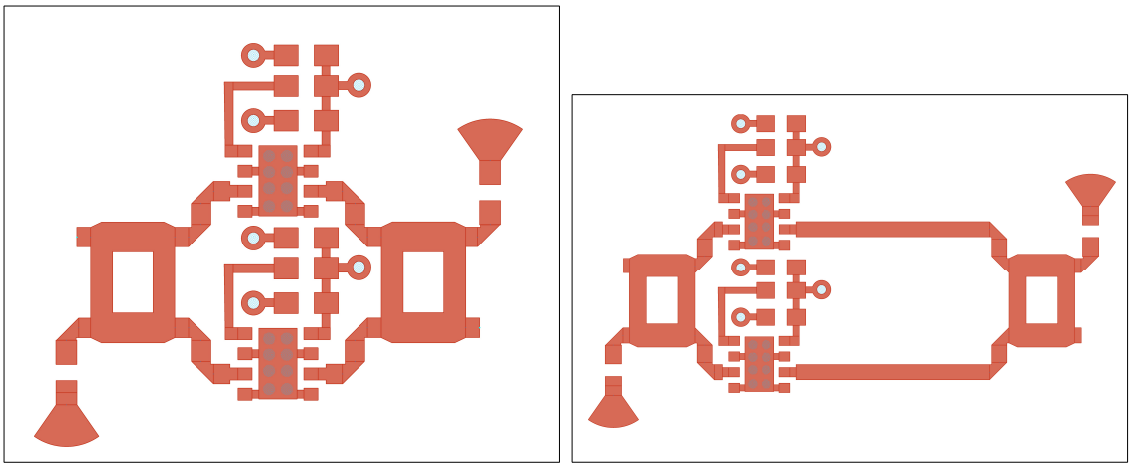

(a) Initial version of the QHC stage **(b)** QHC Stage with optimised distance

Figure 4.11: The initial version of the QHC MAAL configuration

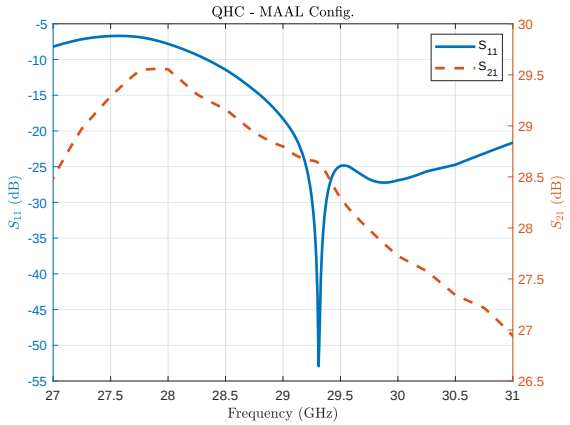

Figure 4.12: S-parameters of QHC implementation

4.4.2 Non-QHC-Based Design Optimisation

For the non-QHC-based implementation, which was intended to be optimised for the entire frequency range, the main optimisation goals were to minimise insertion loss and maximise the output RL. The input RL was not considered, based on the assumption that it would be achieved by maintaining a WR28 isolator at the input of the system chain. As a means to obtain a system alternative that was competitive with the original implementation, a deliberate choice was made to terminate the input and output of the system and each component, with 50 Ω microstrips. The length and widths of the microstrips between input, components and output could then be optimised with the schematic simulator, before being verified using Momentum. Terminating the input and output with 50 Ω attempts to make the system more integrable with other RF systems, where a 50 Ω impedance is a fairly standardised matching impedance.

4.5 Phase 5: Evaluation Board Design

With the layouts for the RF chains completed, work began on designing the layouts for the test board to be manufactured. Since the full implementations exhibited self-oscillations at high gain levels and no mechanical solutions were employed, the evaluation board design was limited to the segments most significant for future testing and measurements.

Figure 4.13 showcases the layout design of the evaluation board. The complete PCB is divided up into four break-off boards, each designed for a different measurement purpose, which are presented in greater detail in Figure 4.14. For this LNA system implementation, achieving a low noise figure is a key system requirement. As the initial stage has the greatest impact on the overall noise figure, the first segment of the QHC design was essential to include for future testing, the layout for which is presented in Figure 4.14(a). We also chose to include a measurement setup for a single MAAL LNA, shown in Figure 4.14(b), so that we could evaluate the QHCs' influence on the overall noise figure and insertion loss. By comparing F and S_{21} from the QHC input setup to the LNA's standalone performance, an accurate comparison between the two could be made. As shown in Figure 4.14(d), we also wanted to include our BS filter to ensure that its simulated performance was well matched by its real-world behaviour.

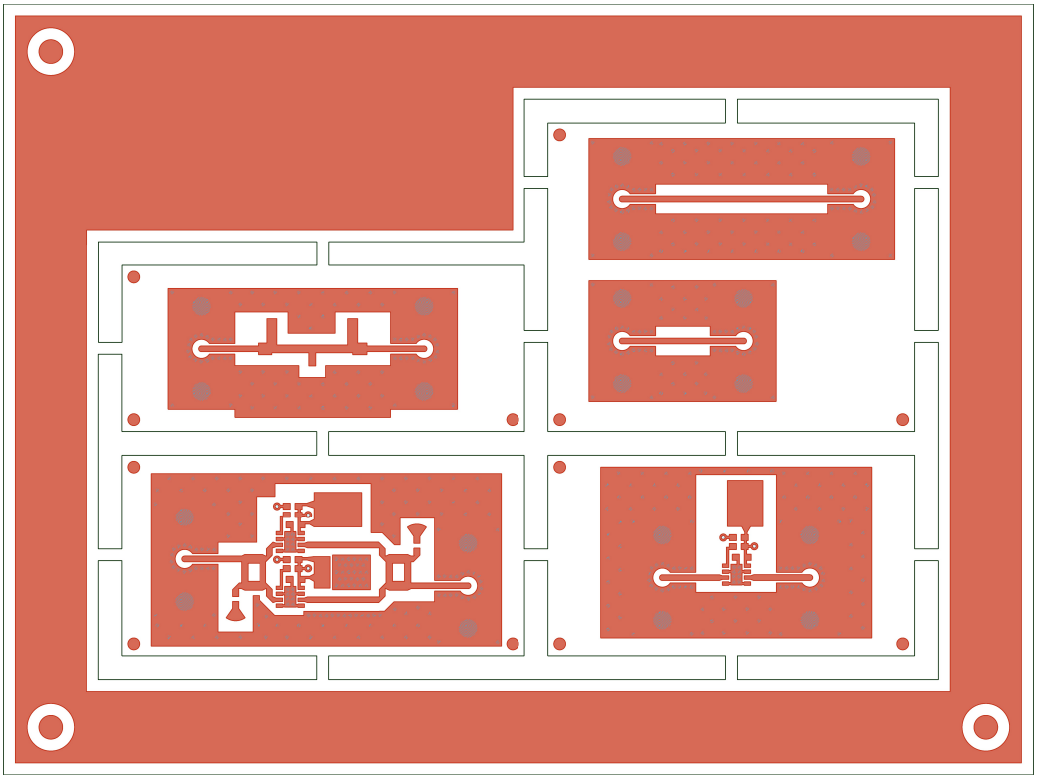

Figure 4.13: Evaluation PCB.

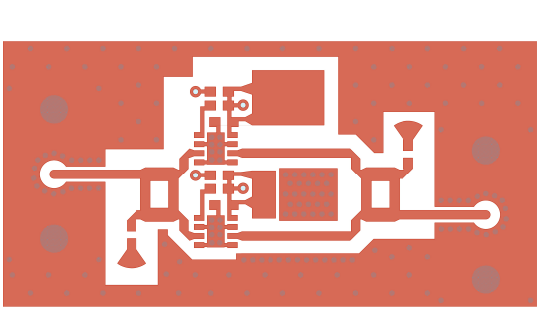

(a) QHC-MAAL Layout

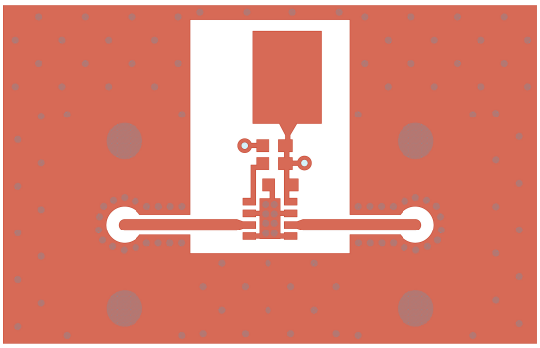

(b) MAAL Layout

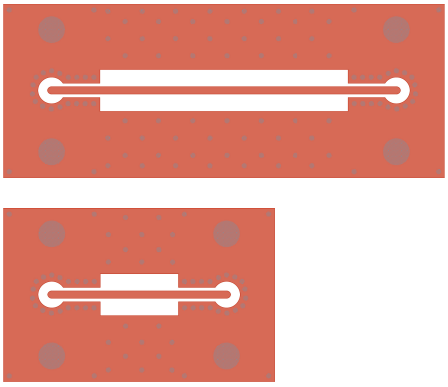

(c) Connector Calibration Layout

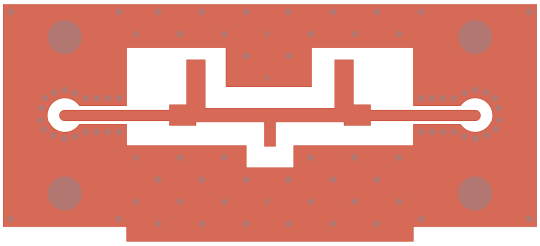

(d) BS Filter Layout

Figure 4.14: Combined layout figures of QHC Stage Final, MAAL Final, Connector Calibration, and BS filter Final

Some noticeable additions to the layout design are the RF measuring connectors and the many vias to ground. The connectors are solderless, which simplifies the testing procedure by removing the necessity to solder on two connectors per evaluation board, and they can instead be re-used between boards using the same screw holes. Ideally, these connectors are supplied with a footprint specifically optimised for the PCB stackup. Unfortunately, these footprints was not provided in time, which required us to design our footprint, with the risk of obtaining an imperfect RL. To assess the expected added insertion loss from the connectors, the setup shown in Figure 4.14(c) was used. The break-off board includes two pairs of connectors, each connected by $50\,\Omega$ microstrips, with one microstrip being twice as long as the other. By comparing the insertion loss of the shorter microstrip to the longer, we can determine the additional loss attributed to the connectors. Since the longer microstrip is expected to have twice the L of the shorter one, the additional loss due to the connectors may be noted.

The numerous vias aim to ensure a solid ground connection around the RF circuit. The Momentum simulator assumes a perfect ground wherever no conductor is present, which implies that the actual ground connection has to be thorough for the real-world behaviour to align with the simulation outputs. Additionally, as mentioned in Section 2.1.3, ground vias also minimise the risk of supporting higher-order modes, which is a key reason for their placement around the RF connectors.

Due to the system's self-oscillations, the cascaded functionality of the components cannot be determined. With the necessary mechanical solutions, the evaluation board should incorporate the chain in its entirety to assess the system's gain, noise figure and OIP3. Since the systems are designed for the lowest possible insertion loss, i.e maximised gain, the cascaded OIP3 was expected to be at its highest, according to (2.26). It would therefore be beneficial to measure the output of the implementations to ensure that the OIP3 remains within the required level and aligns reasonably with the initial calculations performed in Section 4.1. Due to time constraints, an OIP3 measurement setup similar to that of the noise figure measurement could not be properly implemented.

5

System Implementation Results

This chapter presents the final two implementations of the explored low-cost system alternatives to the K_a-band LNA Hybrid, intended for the frequency range of 27 to 31 GHz. For each implementation, the system configuration and layout are detailed, followed by an analysis of their performance across the intended frequency range. The gain and return loss (RL) for each implementation is presented, both in comparison to their respective baseline setups as well as for different attenuation settings. Additionally, concluding remarks are provided regarding each design's noise figure, OIP3 and power consumption. Switching to COTS components and commercial PCB materials, while retaining the WR28 isolators, had the potential to reduce the cost to half that of the original Hi-Rel system. The respective sections will present the additional reduction in cost which could be obtained from removing one or both isolators.

5.1 QHC-Based System Implementation

Figure 5.1 depicts the block diagram of the final QHC-based system implementation, while the layout is shown in Figure 5.2. The dimensions for the various microstrip lines for each segment in the design are listed in Appendix D.1. Its design was optimised for a minimum insertion loss and high return loss at 31 GHz. The system's gain, as well as S_{11} and S_{22}, are showcased in Figure 5.3 for the intended frequency range with zero attenuation. Said metrics are displayed in comparison to the performance of the ideal baseline designs, shown in Figure 4.10.

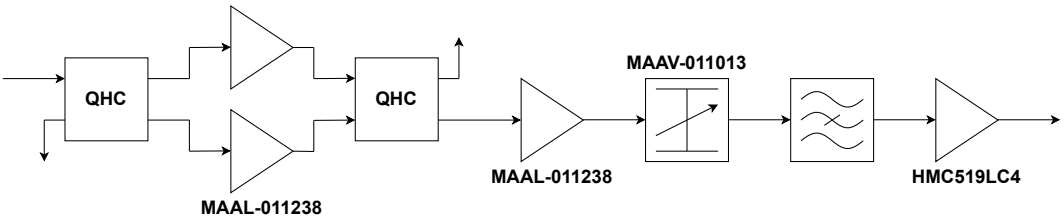

Figure 5.1: Block diagram for QHC implementation of the K_a-band LNA system.

The goal of this implementation was to achieve a system that, through the utilised design strategies, eliminated the need for the expensive WR28 isolators and thus could be considered a cost-effective alternative for LEO satellites. Said strategies aimed to ensure that the noise figure and return loss of the system remained on-par

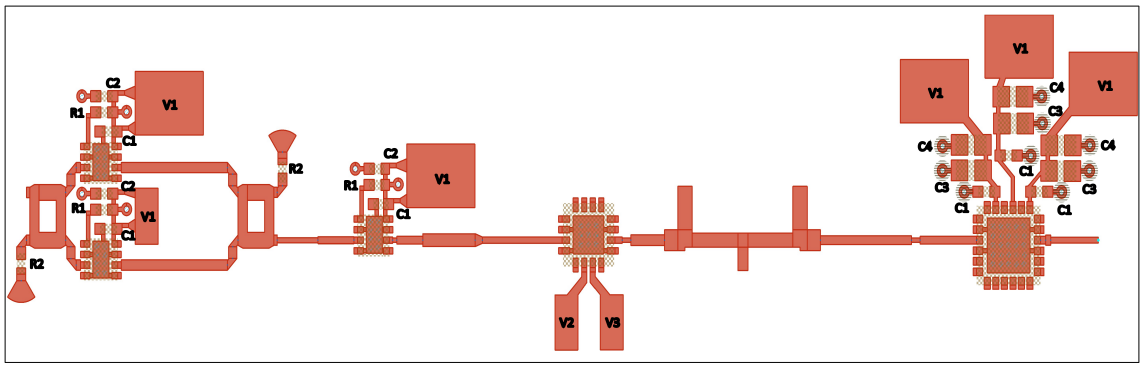

Figure 5.2: Layout of the QHC implementation of the K_a-band LNA system.

to that of the original implementation. Optimising for a minimum L at 31 GHz ensured the lowest possible estimated noise figure, as the actual value could not be simulated due to the noise parameter files not being obtainable. As seen in Figure 5.3(a), this design goal was achieved, with a system gain slightly exceeding the 'ideal' baseline design at the intended frequency. This increase in potential gain is most likely due to the individual components in the ideal baseline configuration not being perfectly matched to 50 Ω. Introducing some variation in impedance with the interconnections between the components most likely resulted in a better impedance match, which in turn allowed more gain to be achieved from the components than what the cascaded Touchstone files in Figure 4.10(a) would suggest.

As mentioned in Section 4.4.1, the inclusion of the QHC-configuration at the input introduced some additional complexity to the design. Ideally, the configuration should behave similarly to the baseline configuration, with a RL as shown in Figure 5.3(b). However, the resulting S_{11} deviated from the expectations, likley due to some sort of coupling between the two QHCs as a consequence of their relatively short distance between eachother. The output return loss, on the other hand was able to fulfill the performance goal of > 16 dB for the majority of the frequency band, as showcased in Figure 5.3(c).

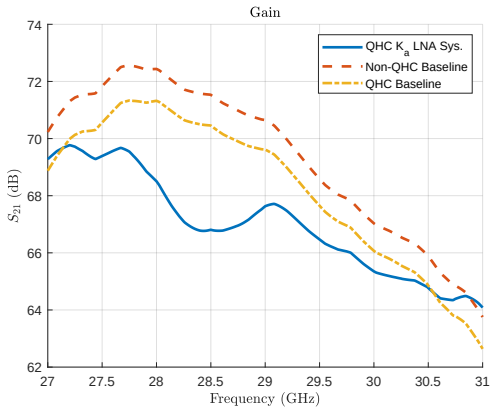

(a) Gain vs Baselines

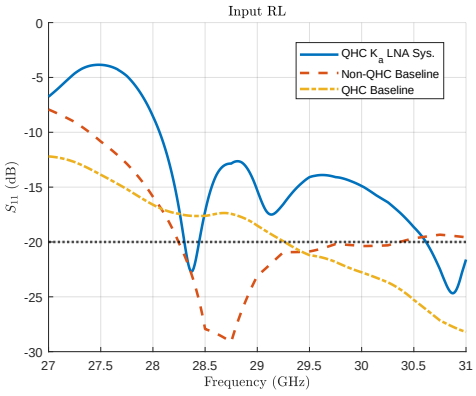

(b) Input RL vs Baselines

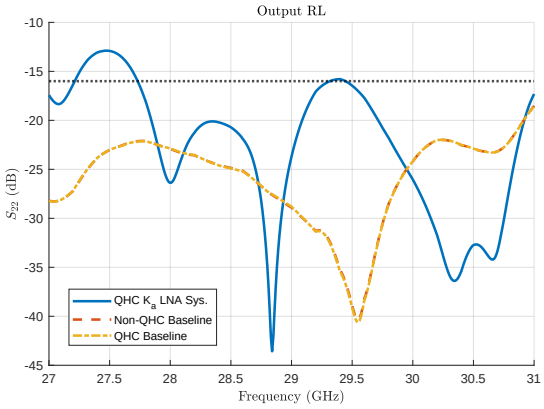

(c) Output RL vs Baselines

Figure 5.3: Comparison of Gain and Return Loss vs Baselines. The orange and yellow curves correspond to the behaviour of the non-QHC baseline and the QHC baseline respectively. The blue curve corresponds to the behaviour of the final QHC-based system implementation.

Figure 5.4 details the variation in system gain, S_{11} and S_{22} for different attenuation settings. *Atten Op. 1* targets a gain of 40 dB at 31 GHz, while *Atten Op. 2 targets* 55 dB. *Max Atten.* indicates the maximum attenuation achievable using the MAAV. As shown in Figure 5.4(a), the LNA system implementation can be adjusted for a gain ranging between 33 to 70 dB. In the common operation range of 40 to 55 dB the system has, at 31 GHz, an average input RL of 24 dB and an average output RL of about 22 dB. In other words, the RL for the output is shown to improve when increasing the level of attenuation, to the point where a majority of frequencies have an RL $>$ 16 dB. The differentiating response in attenuation depends on the setting comes from the S_{22} characteristics of the MAAV [49], which varies depending on the supplied control voltage.

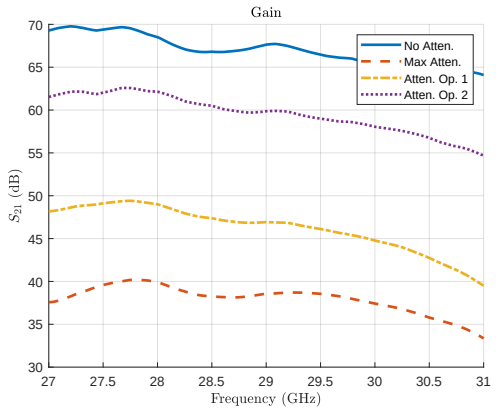

(a) Gain vs Attenuation

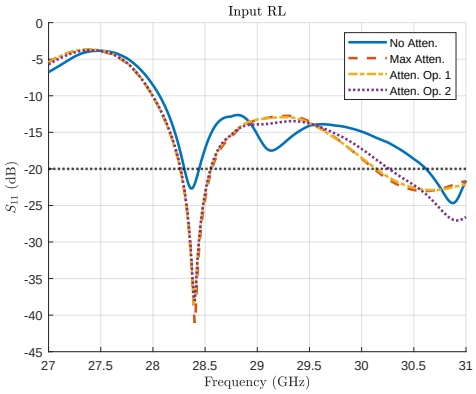

(b) Input RL vs Attenuation

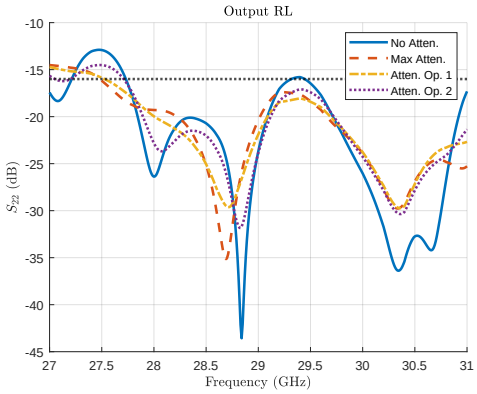

(c) Output RL vs Attenuation

Figure 5.4: Comparison of gain and return loss for the QHC-based design at different attenuation settings. The purple and yellow curves curves correspond to attenuations settings aimed at targeting the upper- and lower levels of the operational gain for the original implementation, i.e 40 and 55 dB respectively.

Figure 5.5 shows the gain and input RL for a wider band of frequencies of the system implementation using QHCs. The figure showcases that the maximum gain is $\sim$ 70 dB, and at 22 GHz, the gain is about -6.3 dB. This implies that the gain

attenuated by approximately 76 dB at 22 GHz, which confirms that the BS filter succeeds in attenuating by at least 50 dB, following the specifications presented in Section 1.4.

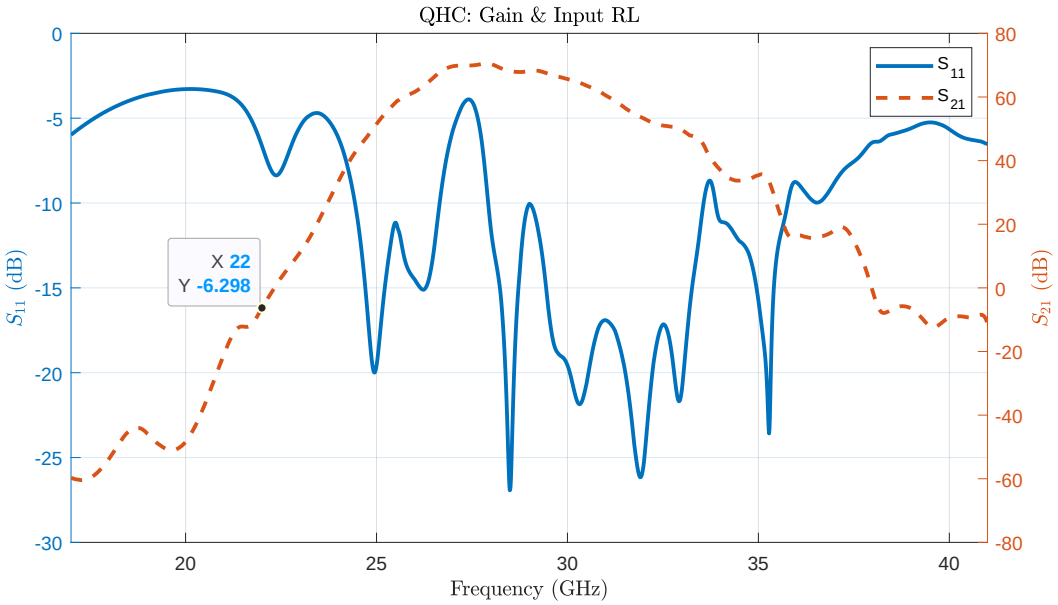

Figure 5.5: QHC implementation gain and input return loss between 17 and 41 GHz

The estimated noise figure of the system implementation is plotted in Figure 5.6. From the graph we can observe that the estimated noise figure ranges from 1.73 to 2.45 dB, with 1.75 dB at 31 GHz. It has an estimated OIP3 of 23 dBm and a power consumption of 0.375 W. By utilising COTS components, Rogers 3003 and by replacing the WR28 isolators with a QHC configuration at the input, while relying on the output RL of the HMC519LC4, the overall cost can be reduced to approximately one tenth of the original implementation.

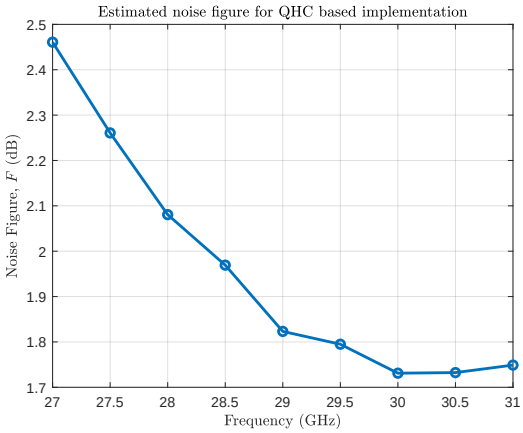

Figure 5.6: Estimated noise figure of QHC-based system implementation.

5.2 Non-QHC-Based System Implementation

Figure 5.7 showcases the block diagram of the final non-QHC based system implementation, and the layout is shown in Figure 5.8. The dimensions for the various microstrip lines for each segment in the design are listed in Appendix D.2. Its design was optimised for a minimum insertion loss and high RL across the entire intended frequency range with the intent of utilising a WR28 isolator at its input. The system's gain, S_{11} and S_{22}, are showcased in Figure 5.9 for the intended frequency range with zero attenuation. Said metrics are displayed in comparison to the performance of the ideal baseline designs.

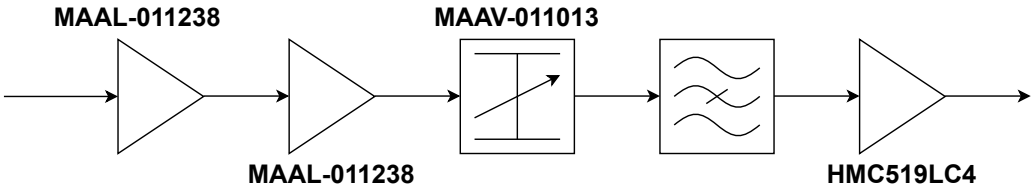

Figure 5.7: Block diagram of the non-QHC implementation of the K_a-band LNA system.

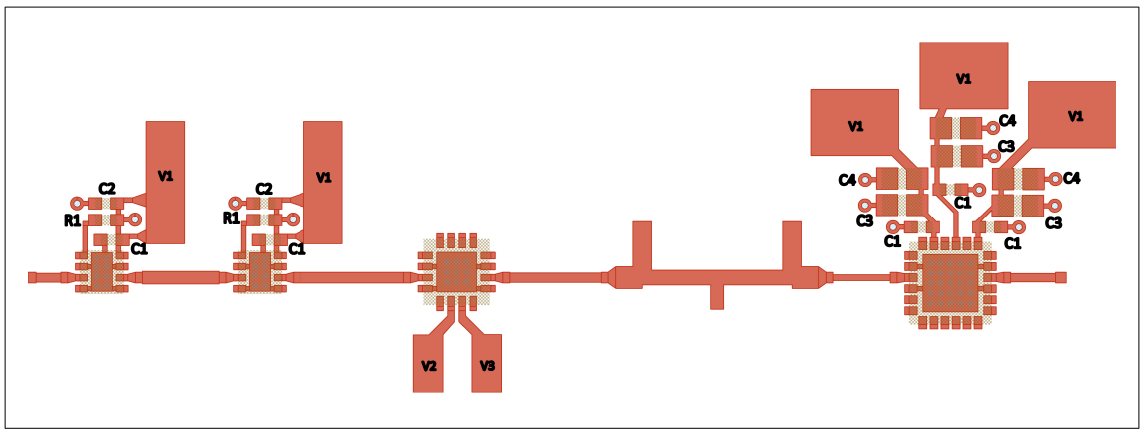

Figure 5.8: Layout of the non-QHC implementation of the K_a-band LNA system. $V1$ corresponds to the systems supply voltage, whereas $V2$ and $V3$ are the attenuator's two control voltages. The values for the biasing components are listed in Appendix E.

Comparing the baseline to what the non-QHC K_a-band LNA system achieved in terms of gain in Figure 5.9(a), we find that some L is introduced between 27 and 30 GHz. Past 30 GHz, however, the designed system gain is higher than the 'ideal' value. Because this system implementation expects to use the WR28 isolators on the input, the requirement of achieving an RL$>$ 20 is not critical. At the output, however, the baseline indicates that the required RL can be met, which is confirmed for the non-QHC implementation, as shown in Figure 5.9(c). This was primarily achieved by adjusting the attenuation level, where attenuation corresponding to the system's operating range in gain ensured a sufficient RL.

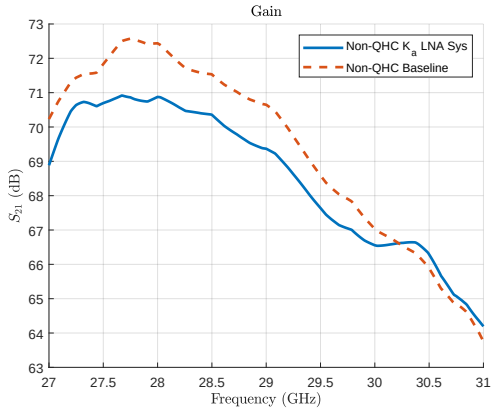

(a) Gain vs Baselines

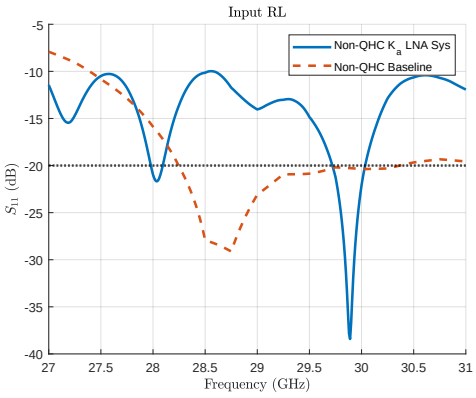

(b) Input RL vs Baselines

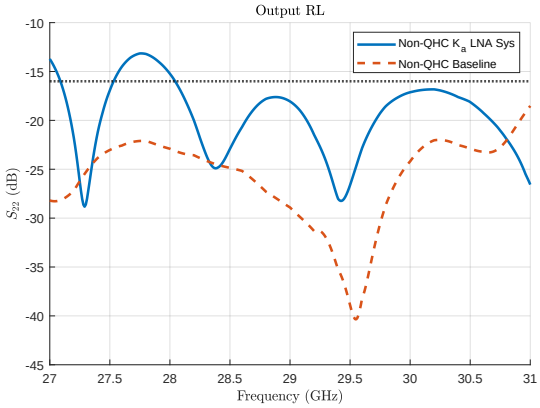

(c) Output RL vs Baselines

Figure 5.9: Comparison of gain and return loss vs baselines. The orange curve correspond to the behaviour of the non-QHC baseline while the blue curve corresponds to the behaviour of the final non-QHC-based system implementation.

Figure 5.10 details the variation in system gain, S_{11} and S_{22} for different attenuation settings. The figure shows that the LNA system implementation can be adjusted for a gain ranging between 40 to 70 dB. In the common operation range of 40 to 55 dB, the system has an input RL $>$ 9 dB, averaging around $\sim$ 15 dB, and an output RL $>$ 18 dB, averaging around $\sim$ 24 dB. The S_{22} improved significantly with increased attenuation and helped the implementation to achieve the performance target across the frequency band. Figure 5.10(a) shows that the attenuated gain seldom drops below 40 dB. Given that the MAAV provides an attenuation range of approximately 40 dB, the gain should ideally be reduced to around 30 dB. Although the system is not intended to operate at such low gain levels, this additional attenuation is necessary for temperature compensation, the secondary purpose of the attenuators. The reason for the decrease in attenuation range is, again, likely due to coupling.

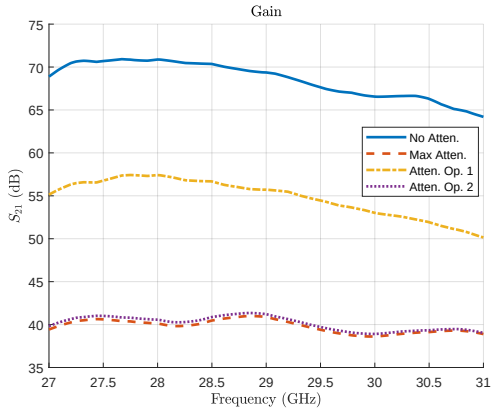

(a) Gain vs Attenuation

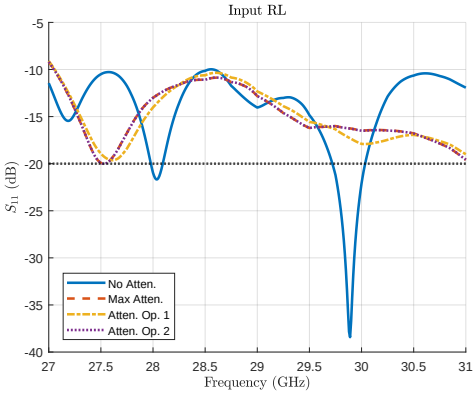

(b) Input RL vs Attenuation

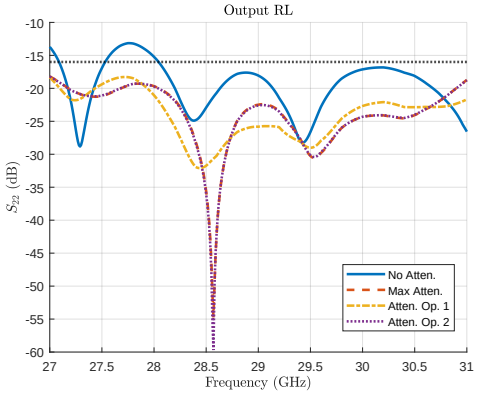

(c) Output RL vs Attenuation

Figure 5.10: Comparison of gain and return loss for the non-QHC-based design at different attenuation settings. The yellow and purple curves curves correspond to attenuations settings aimed at targeting the upper- and lower levels of the operational gain for the original implementation, i.e 40 and 55 dB respectively.

Figure 5.11 shows the gain and input RL for a wider band of frequencies of the non-QHC system implementation. The figure showcases that, thanks to the BS filter, the signal is attenuated by more than 90 dB at 22 GHz, relative to the maximum gain of $\sim$ 70 dB. This is again well above the filter's requirement of a minimum 50 dB attenuation at 22 GHz.

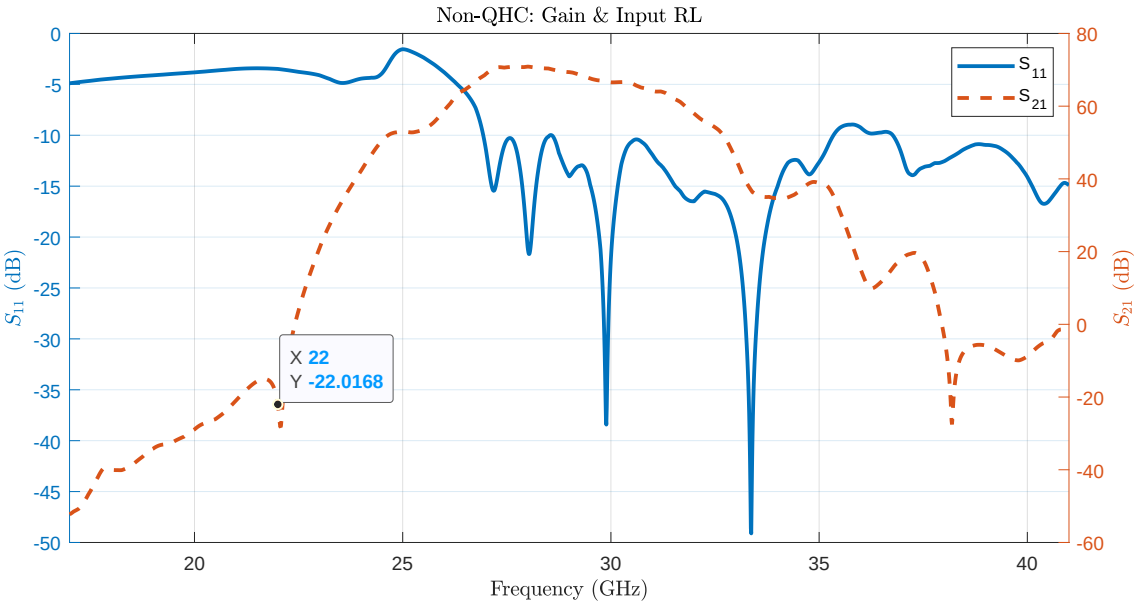

Figure 5.11: Non-QHC implementation gain and input return loss between 17 and 41 GHz

The estimated noise figure of the system implementation is plotted in Figure 5.12. From the graph we can observe that the estimated noise figure ranges from 1.55 to 1.96 dB. Its estimated OIP3 and power consumption is the same as for the QHC-implementation, i.e. 23 dBm and 0.375 W respectively. By utilising COTS components, Rogers 3003 and relying on the output RL of the HMC519LC4, the overall cost can be reduced to approximately one fourth of the original implementation.

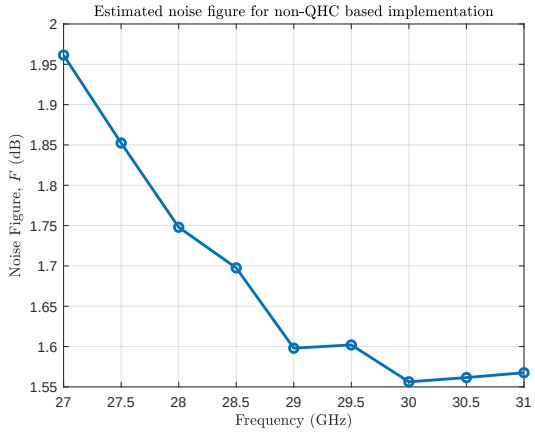

Figure 5.12: Estimated noise figure of non-QHC based system implementation.

6

Discussion

This chapter summarises the various discussions concerning the final system implementations, their potential future improvements, as well as addresses the research questions defined in the project's purpose and goals.

6.1 Evaluation of System Implementations

When compared to the specified system goals, presented in Table 1.2, neither implementation was able to meet all performance metrics across the entire intended frequency range. However, both designs satisfied the requirements for OIP3, power consumption and a sufficient RL at their outputs. The QHC-based system was able to fulfil the requirements for the operational gain, while the non-QHC system was not able to meet the lower end of the operational range for all frequencies. In terms of noise figure, the non-QHC system was able to meet the required performance, but not for the desired level at the lower-end frequencies. The QHC-based system, on the other hand, delivered on the desired noise figure at the upper-end frequencies but fell short at the lower end. This outcome was expected with the decision to optimise the implementation for 31 GHz. Had we optimised for the entire band, we believe a more uniform noise figure could be achieved, averaging around 2.1 dB.

However, it is difficult to make a fair comparison between the two implementations without considering the impact of connecting the WR28 isolator to the input of the non-QHC system. The WR28 isolator is expected to have a slight influence on the system's noise figure and a significant impact on input RL. It would most likely improve the return loss while slightly degrading the noise figure. What can be stated with some certainty is that the QHC, as a replacement for the WR28 isolator, imposes certain design challenges, making it difficult to obtain a sufficient input RL. Although the QHC-based implementation optimised for 31 GHz meets the requirements at the higher frequencies, the expectation is that, if it were optimised for the entire frequency range, it would underperform with input RL values most likely ranging between 15 and 20 dB.

The main challenge throughout the design of the QHC-based implementation was to ensure sufficient system performance while also accommodating the microstrip lines of the QHC-configuration to the component footprints, biasing networks and manufacturer constraints. As stated in Section 4.4.1 concerning the QHC configuration optimisation, there was a design trade-off between high RL and low insertion loss. With the appropriate noise parameter files for the simulations of components,

the configuration may perhaps have been better optimised for high RL while ensuring that the overall noise figure did not exceed the requirements. It is, in other words, difficult to assess the true potential of replacing the WR28 isolators with a microstrip QHC configuration without the noise parameter files.

With the design of the two COTS-based implementations, it is evident that the main trade-offs between cost and performance in this type of LNA system concern the impact on overall system noise figure and input return loss. Assuming the WR28 has minimal impact on the noise figure, we believe the non-QHC implementation strikes the best balance between low-cost and desired performance. With minor adjustments in the design to ensure sufficient adjustable gain across the entire frequency range, such as inserting an additional attenuator, it is capable of meeting all the required system specifications. With the potential to reduce costs to one-fourth of the original system, this implementation demonstrates great promise for the deployment of high-volume satellite constellations. The QHC-based implementation, on the other hand, can be regarded as a baseline which represents the lower bound of performance when prioritising low-cost in the design of an LNA system. At its worst, it exhibited a noise figure about 0.5 dB above, and an RL approximately 16 dB below their respective required level, but allowed for an LNA system that could be manufactured at a cost ten times less than the original implementation.

It should be noted that using a QHC configuration as an isolator is not limited to a COTS-based design. There is also potential to reduce the cost in the Hi-Rel system by switching to a QHC configuration. However, for the system to be better suited to high-volume satellite constellations, it is more beneficial to switch to a design which can be mass-produced using automated machinery. This could not only reduce cost but also, by estimation, potentially allow for a ten times increase in productivity. In a system designed for mass production, it is the WR28 isolator which then represents the most significant portion of the total cost and should therefore be replaced to achieve an even more cost-effective implementation.

6.2 Evaluating Design Options and Methods

In our assessment of the QHC configuration explored, we believe it serves as an appropriate benchmark when evaluating if a design option is suitable for use in an LNA system intended for LEO satellites. For a design option to be deemed suitable, we argue that it must fulfil four criteria: Firstly, it has to offer the potential to reduce cost at a high magnitude for high-volume production. Secondly, it has to meet the system requirements for the majority of the frequency band. As we have learned, the non-linear behaviour of most devices shows that it is difficult to obtain perfect uniform performance across the K_a-band. Still, the expectation from the end-user is that the system should behave linearly across all intended frequencies. Otherwise, they would have to adapt their interconnections between other system modules and the LNA system to its nonlinear behaviour. This, in turn, would limit its range of usability. Thirdly, the design option should not limit the potential of employing other design strategies as a means to reduce cost and/or improve system performance. Lastly, the components and materials used should accommodate the

high levels of radiation present in the intended system environment.

In its current form, the QHC configuration does not meet the required criteria. While it offers significant cost-saving potential by replacing an additional WR28 isolator and does not impose constraints on other explored design options, it fails to meet the performance requirements across most of the K_a-band. However, if it can be optimised to better align with the system specifications of the K_a-band LNA Hybrid, or with another LNA system with less strict requirements, it could be regarded as a suitable design option.

The decision to use an HMC LNA at the output of the two system implementations is another great showcase to evaluate a design option. This choice of encapsulated component not only helps the system be better suited for automated assembly, which decreases production cost, but it also can replace the need for using a WR28 isolator at the output of the amplifier chain, which further reduces cost. The only potential drawback with this component is its relatively large footprint and extensive biasing network, which could limit the design when modifying it to accommodate the interconnection with the system's chassis and external modules. This is, however, difficult to assess at this current stage, so at this moment it fulfils our criteria. Overall, the HMC LNA helps to demonstrate the potential of how COTS components can be selected to achieve balance between cost and performance.

One important note is that our criteria do not consider the extensive testing procedures which should be carried out to assess the systems' reliability to operate in the harsh environment of space. We believe that in the early stages of developing low-cost LNA systems, such as the designs explored throughout this project, it is important to enforce thorough testing procedures to assess the true limits of these types of system implementations. As Jaime Estela remarks, there should be an interest in knowing the true boundaries of the components when operating in LEO [19]. While it is possible to strike a balance between system quality and cost through the number of required reliability tests, the potential cost savings enabled by low-cost RF systems in high-volume satellite constellations should outweigh the initial expenses associated with testing.

The methodologies employed throughout this project were primarily aimed at developing system implementations which eliminated the need for the WR28 isolators, given their substantial impact on overall system cost. However, an alternative design approach could have focused on identifying the lowest possible cost for an LNA system that still relies on these isolators. For example, the substrate evaluation could have been revised to assess the materials' suitability within a non-QHC implementation, using a different microstrip component or segment when comparing their influence on performance. This alternative evaluation might have positioned FR4 as a more viable option, potentially further reducing the system cost associated with circuit board materials. Such an approach could serve as a baseline for potential cost reduction, providing a point of comparison for other design strategies aimed at eliminating the WR28 isolators. Nevertheless, we still believe that the greatest potential to reduce cost lies in replacing the isolators with suitable alternatives.

6.3 Industry Challenges

Our assessment of the industry challenges which hinder the full adoption of the New Space paradigm, specifically in terms of designing LNA systems, are based on its three core principles: commercialism, collaboration and innovation. In our pursuit to develop a low-cost design that meets the required performance metrics, the primary design constraints were rarely related to the components themselves. Instead, we were often constrained by the limited available documentation and data provided by suppliers. Additionally, the current capabilities of the available manufacturing tools also restricted us in what design strategies could be employed, such as the filter design and optimal QHC sizing. We argue that the current conditions concerning the suppliers place a significant strain on the possibilities within collaboration and innovation. This, we also argue, hinders the full embrace of the space paradigm principles when designing LNA systems intended for LEO satellites.

For the most part, we believe this situation will improve over time as increasing interest in COTS-based design options for space applications will likely encourage suppliers to thoroughly test their components and have their data readily available. However, the future concerning the fabrication tools remains uncertain. Developing new manufacturing tools capable of producing the transmission line dimensions required to, for example realise the BP filter, is no easy feat and most likely very costly. Such complex tools may perhaps lead to higher production costs, which goes against the commercialism principle of the New Space paradigm. Ultimately, it would depend on if the cost reduction from the design options would justify the investment into new equipment.

6.4 Future Work

As mentioned in Section 1.6, a complete LNA system for the K_a-band has more requirements other than having sufficient F, G, OIP3 and RL. Finalised product would also need sufficient gain flatness and stability. As shown in Figures 5.3a and 5.9a, the system gain varies heavily, ranging between approximately 64 and 71 dB, for different frequencies, corresponding to a gain flatness of ~ 7 dBpp. This is far-above the usual desired level of 1 dBpp. In our developed system implementations, our focus was on minimising the noise figure. However, with the appropriate component data files, they should be redesigned to also ensure sufficient gain flatness.

As brought up in the discussion of the system implementations, future modifications on the non-QHC design should incorporate an additional attenuator to ensure adequate adjustable gain across the entire frequency range. This addition may also improve the system's ability to compensate for gain fluctuations due to temperature changes, thereby enhancing overall gain stability. To fully assess this, future work should evaluate the system using the necessary S-parameter files corresponding to the different temperatures within the operational range. Simulating the system at different temperature settings would not only provide a broader understanding of its behaviour, but may also help to determine the relevant attenuation range and control logic for the external controller. Most likely the system would have to be

re-designed around the highest expected operating temperature (85 °C) where the attenuator would compensate for any increase in gain as a result of the temperature decreasing. The external controller would also have to be constructed, alongside the power supply module as well as the system chassis and its interconnection to the electronics. Furthermore, the design should also be modified to incorporate mechanical solutions to eliminate any self-induced oscillation, to ensure that the system can operate at the desired higher levels of gain.

Another area that would benefit from future study is the development of BP filters for the K_a-band that conform to the microstrip line restrictions set by the manufacturer. In LNA systems where multiple frequency bands need to be filtered out, it is generally more appropriate to use a single BP filter rather than multiple individual BS filters. While surface-mounted devices may offer a more effective solution, the potential cost savings associated with using microstrip lines to realise the filter could be highly beneficial for high-volume satellite constellations.

As a final note, since we did not have the opportunity to run any tests and measurements on our system, future work should verify the real-life behaviour of the segmented parts incorporated in the evaluation board. The evaluation board could also be updated to incorporate a measuring set-up for the cascaded OIP3 and should also include the necessary mechanical solutions to allow the interconnected system in its entirety to be measured.

6.5 Societal, Ethical, and Ecological Aspects

The purpose of this thesis was to evaluate the possibility of translating a Hi-Rel LNA system to a more cost-effective alternative, which subsequently encourages an increase in the production of LNA systems. This implies the consumption of additional resources in comparison to the limited production of the Hi-Rel systems. The system explored in this thesis uses at least four GaAs MMICs, up to six with a complete and fully functioning QHC implementation, and the additional attenuator required for the complete operating gain. In space applications, these chips and the substrate material are permanently expended resources, as malfunctioned satellites are generally not recovered or recyclable. An additional remark, just as for any RF system intended for satellites, these implementations have the potential to be used within military applications.

The system implementation designs presented in this report are not intended to serve as a direct substitute for the already existing LNA system for the K_a-band. As stated earlier in this chapter, further rigorous testing and design modifications are required before a low-cost alternative can be fully implemented. Additionally, no supply chain analysis has been conducted for the materials and components used in the proposed low-cost implementations. Since the objective for the final low-cost LNA system is to be mass produced, it is especially important to investigate the supply chain to ensure that no component or materials are unethically produced. This is an essential aspect which has to be addressed to ensure responsible manufacturing and traceability of the system.

7

Conclusion

While concerns remain regarding the reliability of using COTS components and commercial circuit board materials, the system implementations developed throughout this project suggest that it is indeed possible to achieve the desired performance with a design more suitable for high-volume production. In addition to using COTS components and substrate materials, the adoption of specific design strategies to replace the WR28 isolators shows considerable promise in reducing overall system cost. The most promising system alternative that meets the required performance specifications eliminates the need for an output isolator and demonstrates the potential to reduce system cost by a factor of four. There is also a significant potential in replacing the isolator component at the input with a QHC configuration, which could contribute to further reducing the cost. However, the challenge remains to find an optimised design which ensures minimal insertion loss while still ensuring high return loss.

An additional challenge when attempting to design, optimise and evaluate different design options concerns the limited available component data as well as the constraints set by PCB manufacturers due to the limitations of their fabrication tools. We argue that this is the main aspect which hinders the full embrace of the New Space paradigm in the context of designing LNA systems. The expectation is that the expanding interest in developing low-cost alternatives for space electronics will encourage suppliers to ensure that the required component data is readily available, improving overall collaboration within the industry. While it is uncertain how suppliers' manufacturing tools could be further developed without increasing production cost, there exist much potential in reducing system cost by incorporating microstrip components as passive devices.

There are many additional stages which have to be carried out until the system can be truly assessed on its relevancy in LEO satellites. With the appropriate component data files, the system could be optimised to better meet the general requirements concerning gain stability and flatness. It would most likely also have to be modified to better accommodate for the interconnection with chassis and submodules. Lastly, we argue that the finalised system should undergo rigorous testing to truly assess the boundaries of the systems in terms of reliability and performance in its expected system environment. While thorough testing may be costly, the potential cost savings with COTS components and associated design strategies for high-volume satellite constellations should justify the investment, particularly as a means to meet the growing demand for low-latency telecommunications and on-demand services.

Use of Generative AI

In this project, generative AI has only been used for mundane tasks such as generating simple MATLAB code for figures and calculations, aiding in the generation of LaTeXtables and helping with the correctness and cohesiveness in the bibliography. Generative AI has also aided with grammatical refinement and suggestions to maintain a cohesive language and flow throughout the report.

Bibliography

[1] A. Durrani, "Top streaming statistics," Aug. 2023, Accessed: 2025-03-28. [Online]. Available: https://www.forbes.com/home-improvement/internet/streaming-stats/

[2] M. Foley, "Evaluation of streaming video usage in a university library before, during, and after the COVID-19 pandemic lockdown," *The Journal of Academic Librarianship*, vol. 49, no. 3, p. 102698, May 2023, DOI: 10.1016/j.acalib.2023.102698.

[3] Netflix, "2024 quarterly earnings," Netflix, Tech. Rep., Jan. 2025, Accessed: 2025-03-27. [Online]. Available: https://ir.netflix.net/financials/quarterly-earnings/default.aspx

[4] A. Lei, "On-demand video content for low latency streaming," Dec. 2024, Accessed: 2025-01-27. [Online]. Available: https://www.byteplus.com/en/topic/75370?title=on-demand-video-content-for-low-latency-streaming

[5] H. Modha, "Why streaming services are investing in live sports," Nov. 2024, Accessed: 2025-03-28. [Online]. Available: https://lsesportsbusiness.org/2024/11/05/why-streaming-services-are-investing-in-live-sports/

[6] A. K. Maini and V. Agrawal, *Satellite Technology: Principles and Applications*, 2nd ed. Chichester, West Sussex, U.K.; Hoboken, N.J.: Wiley, 2011.

[7] J. Foust, "Starlink's disruption of the space industry," May 2024, Accessed: 2025-01-27. [Online]. Available: https://www.thespacereview.com/article/4801/1

[8] Starlink, "Technology - starlink," Jan. 2025, Accessed: 2025-01-27. [Online]. Available: https://www.starlink.com/se/technology

[9] B. Kotnik, D. Selčan, M. Erker, T. Rotovnik, D. Gačnik, G. Furano, and I. Kramberger, "Safe satellite electronics design utilizing COTS components, FDIR techniques, LCL protections, and thorough qualifications," in *2024 IEEE International Symposium on Defect and Fault Tolerance in VLSI and Nanotechnology Systems (DFT)*, 2024, pp. 1–4, DOI: 10.1109/DFT63277.2024.10753553.

[10] J. Budroweit and H. Patscheider, "Risk assessment for the use of COTS devices in space systems under consideration of radiation effects," *Electronics*, vol. 10, no. 9, p. 1008, 2021, DOI: 10.3390/electronics10091008.

[11] J. Lim, A. Nesathurai, B. Nahill, M. Vai, R. Skowyra, K. Bergevin, and P. Gogna, "Assuring the cybersecurity of COTS processors in space systems,"

in *2024 IEEE Physical Assurance and Inspection of Electronics (PAINE)*, 2024, pp. 1–6, DOI: 10.1109/PAINE62042.2024.10792785.

[12] O. Gutiérrez, M. Prieto, A. Perales-Eceiza, A. Ravanbakhsh, M. Basile, and D. Gúzman, "Toward the use of electronic commercial off-the-shelf devices in space: Assessment of the true radiation environment in low earth orbit (LEO)," *Electronics*, vol. 12, no. 19, p. 4058, 2023, DOI: 10.3390/electronics12194058.

[13] J. N. Pelton, *Satellite Communications*, ser. SpringerBriefs in Space Development. New York: Springer, 2012.

[14] Beyond Gravity, "Beyond gravity at a glance," 2025, Accessed: 2025-03-27. [Online]. Available: https://www.beyondgravity.com/en/about

[15] ——, "Beyond gravity: Our locations," 2025, Accessed: 2025-03-27. [Online]. Available: https://www.beyondgravity.com/en/our-locations

[16] ——, "Microwave Communication for Satellites | Beyond Gravity," 2025, Accessed: 2025-03-27. [Online]. Available: https://www.beyondgravity.com/en/satellites/electronic-solutions/microwave

[17] D. M. Pozar, *Microwave and RF Wireless Systems*, 2nd ed. Hoboken, NJ: John Wiley & Sons, Inc., 2001.

[18] M. Pignol, F. Malou, and C. Aicardi, "COTS in space: Constraints, limitations and disruptive capability," in *Radiation Effects on Integrated Circuits and Systems for Space Applications*, R. Velazco, D. McMorrow, and J. Estela, Eds. Cham: Springer International Publishing, 2019, pp. 301–327, DOI: 10.1007/978-3-030-04660-6_12.

[19] J. Estela, "COTS and the NewSpace," in *Radiation Effects on Integrated Circuits and Systems for Space Applications*, R. Velazco, D. McMorrow, and J. Estela, Eds. Cham: Springer International Publishing, 2019, pp. 329–346, DOI: 10.1007/978-3-030-04660-6_13.

[20] H. Ali, A. Ali, M. R. Mughal, L. Reyneri, C. Sansoe, and J. Praks, "Modular design of RF front end for a Nanosatellite communication subsystem tile using low-cost commercial components," *International Journal of Aerospace Engineering*, vol. 2019, no. 1, p. 8174158, 2019, DOI: 10.1155/2019/8174158.

[21] "Waveguide Sizes | Dimensions & Cutoff Frequency - everything RF," Accessed: 2025-05-07. [Online]. Available: https://www.everythingrf.com/tech-resources/waveguides-sizes

[22] D. M. Pozar, *Microwave Engineering*, 4th ed. Hoboken, NJ: John Wiley & Sons, Inc., 2012.

[23] H. Kumar and E. S. Gopi, Eds., *RF, Microwave and Millimeter Wave Technologies*, 1st ed., ser. Signals and Communication Technology. Cham: Springer Nature Switzerland, 2024.

[24] C. W. Sayre, *Complete Wireless Design*, 2nd ed., ser. McGraw-Hill's AccessEngineering. New York: McGraw-Hill, 2008.

[25] C. Bowick, J. Blyler, and C. J. Ajluni, *RF Circuit Design*, 2nd ed. Amsterdam, Boston: Newnes/Elsevier, 2008.

[26] T. Edwards and M. B. Steer, *Foundations for Microstrip Circuit Design*, 4th ed. Chichester, West Sussex, United Kingdom: John Wiley & Sons Inc, 2016.

[27] M. A. Morgan, *Principles of RF and Microwave Design*, ser. Artech House Microwave Library. Norwood, MA: Artech House, 2020.

[28] M. Božanić and S. Sinha, *Millimeter-Wave Low Noise Amplifiers*, 1st ed., ser. Signals and Communication Technology. Cham: Springer International Publishing, 2018.

[29] M. Almalkawi, *RF and Microwave Module Level Design and Integration*. Institution of Engineering and Technology (The IET), 2019.

[30] D. Sharma and P. Shanthi, "Design & implementation of microstrip interdigital band-pass filter for X-band applications," in *2022 IEEE 3rd Global Conference for Advancement in Technology (GCAT)*, 2022, pp. 1–6, DOI: 10.1109/GCAT55367.2022.9972048.

[31] M. H. Sadok, Y. Lamhene, S. Berkani, and H. Baudrand, "Design of a planar band-stop filter based on stub technique," in *2017 International Conference on Wireless Technologies, Embedded and Intelligent Systems (WITS)*, 2017, pp. 1–5, DOI: 10.1109/WITS.2017.7934680.

[32] P. Pramanick and P. Bhartia, *Modern RF and Microwave Filter Design*, ser. Artech House Microwave Library. Boston, London: Artech House, 2016.

[33] M. Dong, *RF Circuits and Applications for Practicing Engineers*, ser. Artech House Microwave Library. Boston, London, Norwood: Artech House, 2021.

[34] C. Coombs and H. Holden, *Printed Circuits Handbook*, 7th ed. New York, N.Y.: McGraw-Hill Education, 2016.

[35] H. Spieler, *Semiconductor Detector Systems*. Oxford University Press, Aug. 2005.

[36] R. Zuleeg, "Radiation effects in GaAs FET devices," *Proceedings of the IEEE*, vol. 77, no. 3, pp. 389–407, Mar. 1989, DOI: 10.1109/5.24126.

[37] H. Ohyama, E. Simoen, S. Kuroda, C. Claeys, Y. Takami, T. Hakata, K. Kobayashi, M. Nakabayashi, and H. Sunaga, "Degradation and recovery of AlGaAs/GaAs p-HEMT irradiated by high-energy particle," *Microelectronics Reliability*, vol. 41, no. 1, pp. 79–85, Jan. 2001, DOI: 10.1016/S0026-2714(00)00073-1.

[38] M. Takikawa and K. Joshin, "Pseudomorphic n-InGaP/InGaAs/GaAs high electron mobility transistors for low-noise amplifiers," *IEEE Electron Device Letters*, vol. 14, no. 8, pp. 406–408, Aug. 1993, DOI: 10.1109/55.225594.

[39] M. A. Alim and A. A. Rezazadeh, "Device behaviour and zero temperature coefficients analysis for microwave GaAs HEMT," *Solid-State Electronics*, vol. 147, pp. 13–18, Sep. 2018, DOI: 10.1016/j.sse.2018.06.004.

[40] Y. Jin, Z. Wang, and J. Chen, *Introduction to Microsystem Packaging Technology*. CRC Press, Dec. 2017.

[41] R. Tummala, *Fundamentals of Device and Systems Packaging: Technologies and Applications*, 2nd ed. New York, N.Y: McGraw-Hill Education, 2019.

[42] C. A. Harper, Ed., *Electronic Materials and Processes Handbook*, 3rd ed., ser. McGraw-Hill Handbooks. New York: McGraw-Hill, 2003.

[43] Cicor, "Substrates and hybrid circuits," 2025, Accessed: 2025-03-14. [Online]. Available: https://www.cicor.com/fileadmin/user_upload/07_Files/Factsheets/Cicor_Substrates_and_hybrid_circuits_EN.pdf

[44] Keysight Technologies, "Advanced design system 2019 update 1 release notes," Keysight Technologies, Tech. Rep., 2019, Accessed: 2025-03-14. [Online]. Available: https://edadownload.software.keysight.com/eedl/ads/2019update1/pdf/Release_Notes.pdf?PRODUCT_TYPE=PDF

[45] ——. Momentum key features. Accessed: 2025-04-15. [Online]. Available: https://www.keysight.com/us/en/lib/resources/training-materials/momentum-key-features-1936424.html

[46] Macom, "MAAL-011238 datasheet," Accessed: 2025-05-12. [Online]. Available: https://www.macom.com/products/product-detail/MAAL-011238

[47] R. Velazco, *Radiation Effects on Integrated Circuits and Systems for Space Applications*. Cham: Springer International Publishing AG, 2019.

[48] Analog Devices, "HMC519LC4 datasheet," Accessed: 2025-05-12. [Online]. Available: https://www.analog.com/en/products/hmc519lc4.html

[49] Macom, "MAAV-011013 datasheet," Accessed: 2025-05-12. [Online]. Available: https://www.macom.com/products/product-detail/MAAV-011013

[50] Isola Group, "370HR laminate and prepreg data sheet," 2017, Accessed: 2025-02-14. [Online]. Available: https://www.isola-group.com/wp-content/uploads/data-sheets/370hr-laminate-prepreg.pdf?t=1138084184

[51] Rogers Corporation, "RO3000 series laminates data sheet," 2023, Accessed: 2025-02-14. [Online]. Available: https://www.rogerscorp.com/advanced-electronics-solutions/ro3000-series-laminates

[52] ——, "RO4350B laminates data sheet," 2023, Accessed: 2025-02-14. [Online]. Available: https://www.rogerscorp.com/advanced-electronics-solutions/ro4000-series-laminates/ro4350b-laminates

A

List of Components Investigated

Table A.1: COTS RF amplifier components investigated with relevant specifications.

Component	**Supplier**	F **(dB)**	G **(dB)**	**OIP3 (dBm)**	**RL [In/Out](dB)**
MAAL-011238	Macom	1.2	30	20	10/10
MAAL-011240	Macom	1.2	25	15	12/15
HMC519LC4	Analog Devices	3.0	14	24	17/22
ADL8142	Analog Devices	1.6	27	21.5	13/15
ADL8142S	Analog Devices	1.6	27	21.5	13/15
QPA2628	Qorvo	1.6	23	27	11/16
HMC1040LP3CE	Analog Devices	2.2	23	22	12/13
HMC263LP4E	Analog Devices	2.2	19	18	9/9
ADL8106	Analog Devices	3.0	20	21	13/16

Table A.2: COTS RF attenuator components investigated with relevant specifications.

Component	**Supplier**	L **(dB)**	**Max Attenuation (dB)**	**RL [In/Out] (dB)**
TGL4203-SM	Qorvo	3.5	15	15/15
HMC985ALP4KE	Analog Devices	2.1	39	13/13
MAAT-010521-H1	Macom	3.0	27	10/10
MAAV-011013	Macom	2.5	30	10/10
TGL2767-SM	Qorvo	1.6	19	12/12
CHT4694-QAG	UMS	4.0	22	10/6
HMC939ALP4E	Analog Devices	6.0	31	10/10

B

List of Substrates Investigated

Table B.1: Properties of various PCB materials that are available to order from Cogra.

Material	**Composite**	ϵ_r (10 GHz)	D_f (10 GHz)
FR4 (370HR [50])	Fiberglass + epoxy resin	3.92	0.0250
FR4 (DE104)	Fiberglass + epoxy resin	4.32 (5 GHz)	0.024 (5 GHz)
Rogers (RO3003 [51])	Ceramic + PTFE	3.00	0.0010
Rogers (RO3006)	Ceramic + PTFE	6.15	0.0020
Rogers (RO3010 [51])	Ceramic + PTFE	10.20	0.0022
Rogers (RO3035)	Ceramic + PTFE	3.50	0.0015
Rogers (RO4350B [52])	Woven glass + hydrocarbon/ceramics	3.48	0.0037
Rogers (RO4003C)	Woven glass + hydrocarbon/ceramics	3.38	0.0027
Rogers (DiClad 527)	Fiberglass + PTFE	2.5	0.0017
Rogers (DiClad 880)	Fiberglass + PTFE	2.20	0.0009

C

Results From Component Configuration Screenings

Table C.1: Naming convention for components used within different system configurations as a means to improve readability in the following result table.

Component Name	Component ID
MAAL-011238	L01
MAAL-011240	L02
HMC519LC4	L03
ADL8142	L04
ADL8142S	L05
QPA2628	L06
HMC1040LP3CE	L07
HMC263LP4E	L08
ADL8106	L09
HMC985ALP4KE	A01
MAAT-010521-H1	A02
MAAV-011013	A03
TGL2767-SM	A04

C.1 Results From Initial Configuration Screening

Table C.2: Generated list of possible component configurations from the initial screening procedure. The configuration name corresponds to the component selection for slot A, B and C respectively as showcased in Figure 4.1.

Component Data						
Name	**Gain**	**F**	**OIP3**	**Bias Current [mA]**	**Cost**	**Power [W]**
L01,L01,A01	114	1.50	19.99	150	5358	0.45
L01,L01,A02	112	1.50	19.99	150	5206	0.45
L01,L01,A03	113	1.50	19.99	150	4713	0.45
L01,L01,A04	115	1.50	19.99	150	6032	0.45
L01,L04,A01	105	1.50	21.48	150	4491	0.45

Component Data (Continued)						
Name	**Gain**	**F**	**OIP3**	**Bias Current [mA]**	**Cost**	**Power [W]**
L01,L04,A02	103	1.50	21.47	150	4338	0.45
L01,L04,A03	104	1.50	21.47	150	3846	0.45
L01,L04,A04	106	1.50	21.48	150	5165	0.45
L01,L05,A01	105	1.50	21.48	150	6171	0.45
L01,L05,A02	103	1.50	21.47	150	6019	0.45
L01,L05,A03	104	1.50	21.47	150	5527	0.45
L01,L05,A04	106	1.50	21.48	150	6845	0.45
L04,L01,A01	111	1.60	19.99	150	4924	0.45
L04,L01,A02	109	1.60	19.99	150	4772	0.45
L04,L01,A03	110	1.60	19.99	150	4280	0.45
L04,L01,A04	112	1.60	19.99	150	5598	0.45
L04,L04,A01	102	1.60	21.48	150	4057	0.45
L04,L04,A02	100	1.60	21.47	150	3904	0.45
L04,L04,A03	101	1.60	21.47	150	3412	0.45
L04,L04,A04	103	1.60	21.48	150	4731	0.45
L04,L05,A01	102	1.60	21.48	150	5737	0.45
L04,L05,A02	100	1.60	21.47	150	5585	0.45
L04,L05,A03	101	1.60	21.47	150	5093	0.45
L04,L05,A04	103	1.60	21.48	150	6412	0.45
L05,L01,A01	111	1.60	19.99	150	5765	0.45
L05,L01,A02	109	1.60	19.99	150	5612	0.45
L05,L01,A03	110	1.60	19.99	150	5120	0.45
L05,L01,A04	112	1.60	19.99	150	6439	0.45
L05,L04,A01	102	1.60	21.48	150	4897	0.45
L05,L04,A02	100	1.60	21.47	150	4745	0.45
L05,L04,A03	101	1.60	21.47	150	4252	0.45
L05,L04,A04	103	1.60	21.48	150	5571	0.45
L05,L05,A01	102	1.60	21.48	150	6578	0.45
L05,L05,A02	100	1.60	21.47	150	6425	0.45
L05,L05,A03	101	1.60	21.47	150	5933	0.45
L05,L05,A04	103	1.60	21.48	150	7252	0.45

C.2 Results From Final Configuration Screening

Table C.3: Generated list of possible component configurations which has MAAL-011238 as its first LNA. The configuration name corresponds to the component selection for slot B, C, E respectively as showcased in Figure 4.2.

Component Data					
Name	**Gain**	**F**	**OIP3**	**Power [W]**	**Cost**
L01, L06, A04	81	1.50	26.83	0.42	4281
L01, L06, A01	80	1.50	26.81	0.42	3944
L01, L06, A03	80	1.50	26.79	0.42	3622
L01, L06, A02	79	1.50	26.77	0.42	3868
L04, L06, A04	78	1.50	26.88	0.42	4064
L05, L06, A04	78	1.50	26.88	0.42	4485
L04, L06, A01	77	1.50	26.86	0.42	3727
L05, L06, A01	77	1.50	26.86	0.42	4148
L04, L06, A03	77	1.50	26.85	0.42	3405
L05, L06, A03	77	1.50	26.85	0.42	3825
L04, L06, A02	76	1.50	26.83	0.42	3651
L05, L06, A02	76	1.50	26.83	0.42	4071
L02, L06, A04	76	1.50	26.48	0.615	4293
L02, L06, A01	75	1.50	26.42	0.615	3956
L02, L06, A03	75	1.50	26.37	0.615	3633
L02, L06, A02	74	1.50	26.30	0.615	3879
L06, L06, A04	74	1.50	26.96	0.615	4833
L07, L06, A04	74	1.50	26.89	0.555	4466
L06, L06, A01	73	1.50	26.96	0.615	4496
L07, L06, A01	73	1.50	26.88	0.555	4129
L06, L06, A03	73	1.50	26.96	0.615	4173
L07, L06, A03	73	1.50	26.87	0.555	3807
L06, L06, A02	72	1.50	26.95	0.615	4420
L07, L06, A02	72	1.50	26.85	0.555	4053
L01, L03, A04	72	1.50	23.36	0.375	3976
L01, L03, A01	71	1.50	23.29	0.375	3639
L01, L03, A03	71	1.50	23.22	0.375	3317
L09, L06, A04	71	1.50	26.86	0.705	5101
L01, L03, A02	70	1.50	23.14	0.375	3563
L09, L06, A01	70	1.50	26.85	0.705	4764
L09, L06, A03	70	1.50	26.83	0.705	4442
L08, L06, A04	70	1.50	26.73	0.519	4642
L09, L06, A02	69	1.50	26.81	0.705	4688
L08, L06, A01	69	1.50	26.70	0.519	4305
L08, L06, A03	69	1.50	26.67	0.519	3983
L04, L03, A04	69	1.50	23.53	0.375	3759

Component Data (Continued)					
Name	**Gain**	**F**	**OIP3**	**Power [W]**	**Cost**
L05, L03, A04	69	1.50	23.53	0.375	4180
L08, L06, A02	68	1.50	26.63	0.519	4229
L04, L03, A01	68	1.50	23.48	0.375	3422
L05, L03, A01	68	1.50	23.48	0.375	3843
L04, L03, A03	68	1.50	23.43	0.375	3100
L05, L03, A03	68	1.50	23.43	0.375	3520
L04, L03, A02	67	1.50	23.37	0.375	3346
L05, L03, A02	67	1.50	23.37	0.375	3766
L03, L06, A04	65	1.50	26.92	0.57	4528
L06, L03, A04	65	1.50	23.86	0.57	4528
L07, L03, A04	65	1.50	23.58	0.51	4161
L03, L06, A01	64	1.50	26.92	0.57	4191
L06, L03, A01	64	1.50	23.84	0.57	4191
L07, L03, A01	64	1.50	23.53	0.51	3824
L03, L06, A03	64	1.50	26.91	0.57	3868
L06, L03, A03	64	1.50	23.83	0.57	3868
L07, L03, A03	64	1.50	23.49	0.51	3502
L03, L06, A02	63	1.50	26.90	0.57	4115
L06, L03, A02	63	1.50	23.81	0.57	4115
L07, L03, A02	63	1.50	23.43	0.51	3748
L09, L03, A04	62	1.50	23.48	0.66	4796
L09, L03, A01	61	1.50	23.42	0.66	4459
L09, L03, A03	61	1.50	23.36	0.66	4137
L08, L03, A04	61	1.50	23.02	0.474	4337
L09, L03, A02	60	1.50	23.29	0.66	4383
L03, L03, A04	56	1.50	23.71	0.525	4223
L03, L03, A01	55	1.50	23.67	0.525	3886
L03, L03, A03	55	1.50	23.64	0.525	3563
L03, L03, A02	54	1.50	23.60	0.525	3810

D

Drawings of Microstrip Lines for System Implementations

This appendix contains drawings and tables displaying the different dimensions of the Microstrip lines designed to achieve each implementation's system behaviour.

D.1 Microstrip Lines for QHC-Based System Implementation

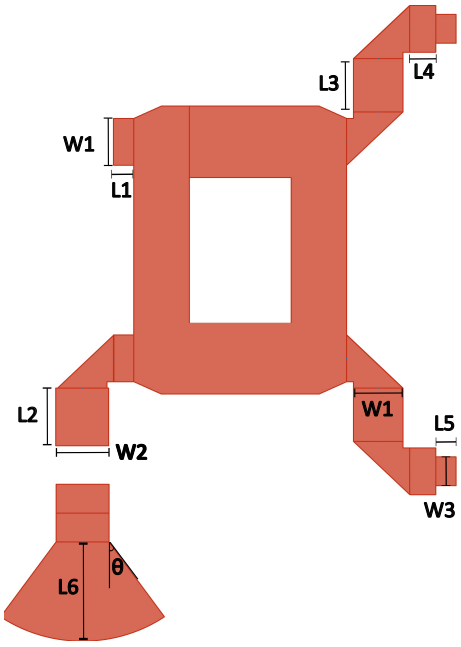

Figure D.1: Microstrip line segment 1.1.

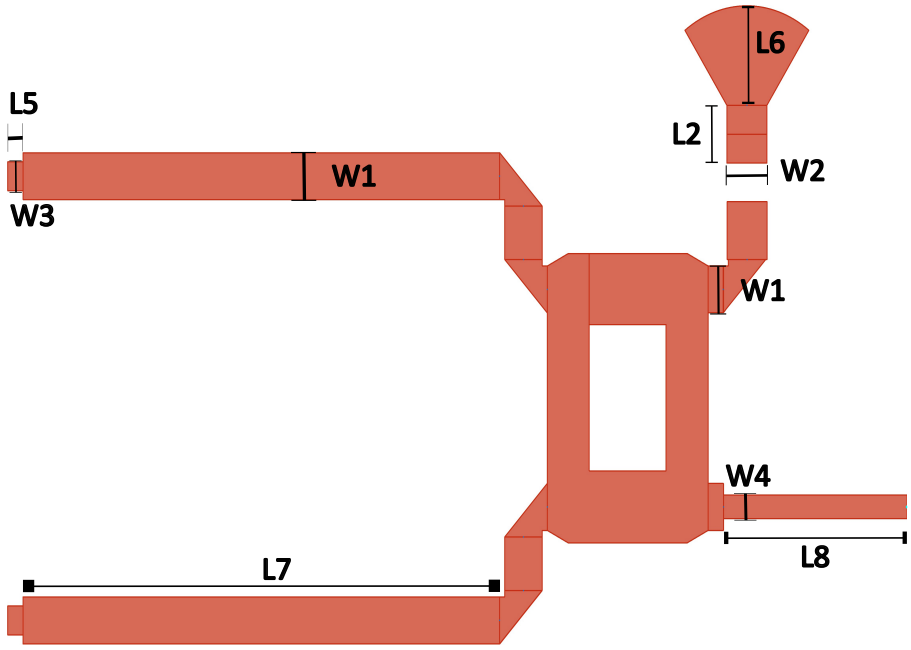

Figure D.2: Microstrip line segment 1.2

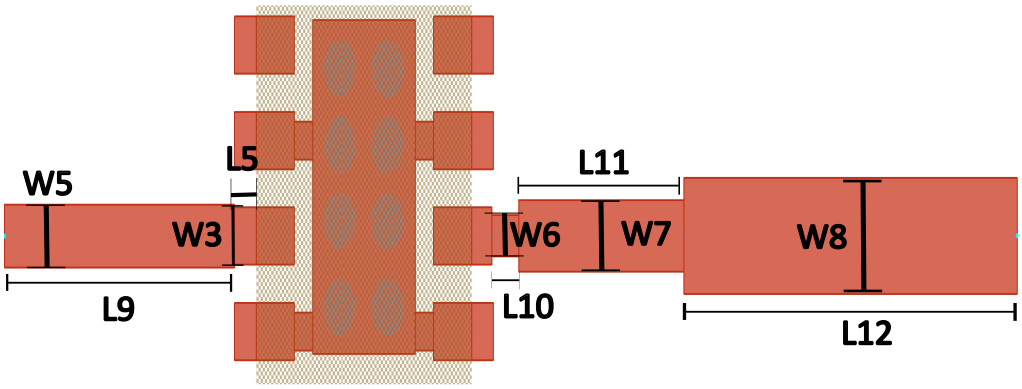

Figure D.3: Microstrip line segment 1.3

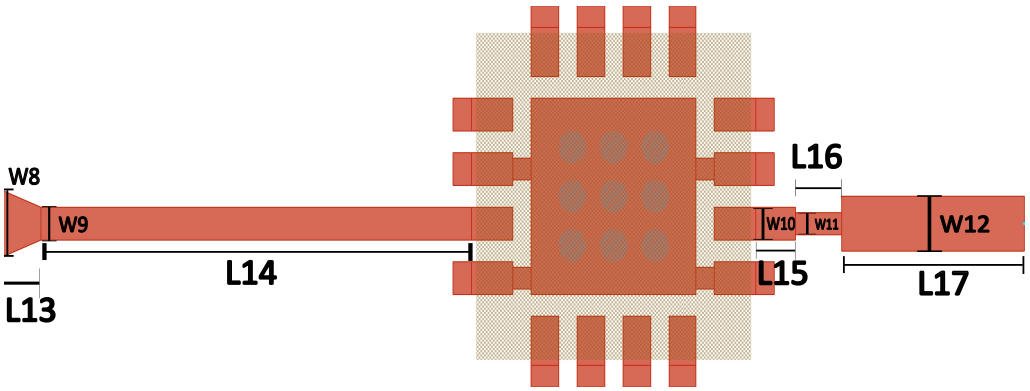

Figure D.4: Microstrip line segment 1.4

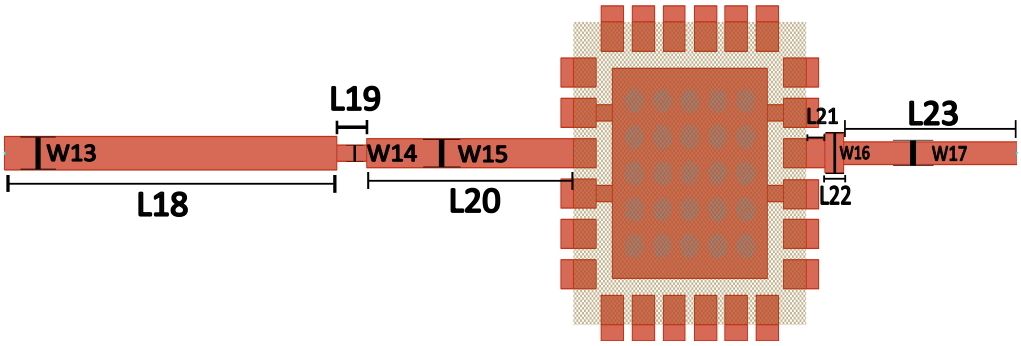

Figure D.5: Microstrip line segment 1.5

Table D.1: Widths and lengths of microstrip line sections for QHC-based system implementation.

Parameter	**Value**
Widths	**(mm)**
W1	0.4860
W2	0.5200
W3	0.3000
W4	0.2438
W5	0.3296
W6	0.2158
W7	0.3750
W8	0.6072
W9	0.3000
W10	0.3000
W11	0.2026
W12	0.5036
W13	0.4136
W14	0.2000
W15	0.3600
W16	0.4864
W17	0.2800
Lengths	**(mm)**
L1	0.1884
L2	0.6000
L3	0.5543
L4	0.2560
L5	0.2000
L6	1.0318
L7	6.2297
L8	2.3850
L9	2.1135
L10	0.2473
L11	1.5249
L12	3.0719
L13	0.4167
L14	4.6780
L15	0.4305
L16	0.5007
L17	1.9804
L18	5.3341
L19	0.5062
L20	3.3175
L21	0.3000
L22	0.3000
L23	2.7870
Angles	**(°)**
θ	35

D.2 Microstrip Lines for Non-QHC Based System Implementation

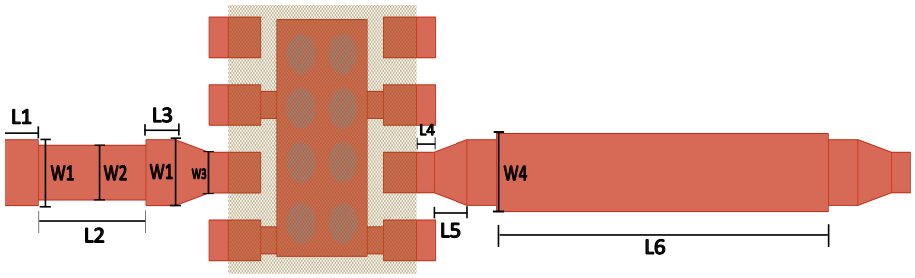

Figure D.6: Microstrip line segment 2.1

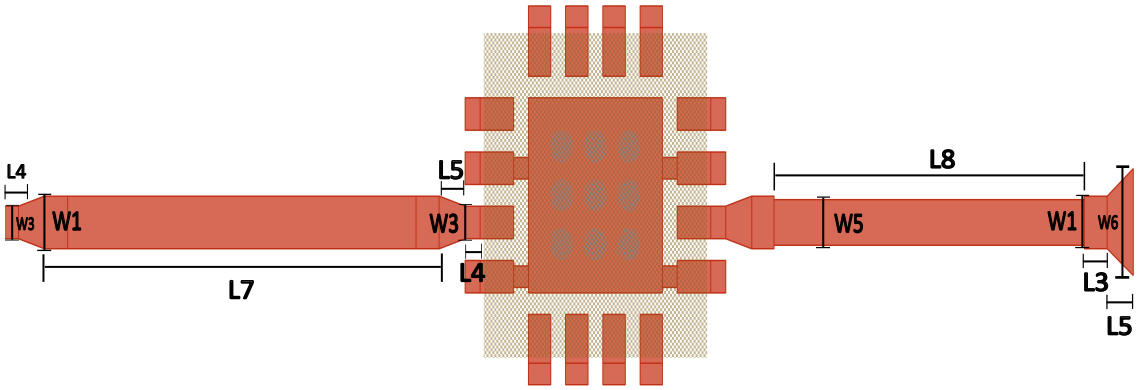

Figure D.7: Microstrip line segment 2.2

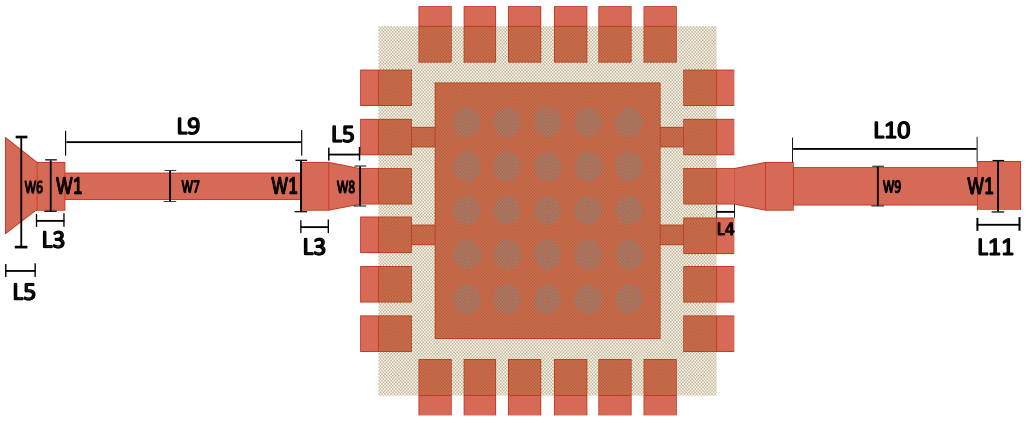

Figure D.8: Microstrip line segment 2.3

Table D.2: Widths and lengths of microstrip line sections for non-QHC-based system implementation.

Parameter	**Value**
Widths	**(mm)**
W1	0.4860
W2	0.4038
W3	0.3000
W4	0.5772
W5	0.4222
W6	0.9858
W7	0.2702
W8	0.3600
W9	0.3820
Lengths	**(mm)**
L1	0.3694
L2	1.1249
L3	0.3088
L4	0.2000
L5	0.3500
L6	3.4801
L7	4.7026
L8	4.1823
L9	2.6208
L10	2.0365
L11	0.4843

E

Bias Network Components

Table E.1: Component values used in biasing networks for the final system implementations.

Parameter	**Value**
Resistors	**(Ω)**
R1	500
R2	50
Capacitors	**(F)**
C1	100p
C2	0.1μ
C3	1000p
C4	4.7μ